

Demonstration of quantum error correction and universal gate set on a binomial bosonic logical qubit

L. Hu,^{1,*} Y. Ma,^{1,*} W. Cai,¹ X. Mu,¹ Y. Xu,¹ W. Wang,¹ Y. Wu,² H. Wang,¹
Y. P. Song,¹ C.-L. Zou,^{3,†} S. M. Girvin,⁴ L.-M. Duan,^{1,2} and L. Sun^{1,‡}

¹Center for Quantum Information, Institute for Interdisciplinary Information Sciences, Tsinghua University, Beijing 100084, China

²Department of Physics, University of Michigan, Ann Arbor, Michigan 48109, USA

³Key Laboratory of Quantum Information, CAS, University of Science and Technology of China, Hefei, Anhui 230026, P. R. China

⁴Departments of Applied Physics and Physics, Yale University, New Haven, CT 06511, USA

Logical qubit encoding and quantum error correction (QEC) have been experimentally demonstrated in various physical systems with multiple physical qubits, however, logical operations are challenging due to the necessary nonlocal operations. Alternatively, logical qubits with bosonic-mode-encoding are of particular interest because their QEC protection is hardware efficient, but gate operations on QEC protected logical qubits remain elusive. Here, we experimentally demonstrate full control on a single logical qubit with a binomial bosonic code, including encoding, decoding, repetitive QEC, and high-fidelity (97.0% process fidelity on average) universal quantum gate set on the logical qubit. The protected logical qubit has shown 2.8 times longer lifetime than the uncorrected one. A Ramsey experiment on a protected logical qubit is demonstrated for the first time with two times longer coherence than the unprotected one. Our experiment represents an important step towards fault-tolerant quantum computation based on bosonic encoding.

Quantum states are fragile and can be easily destroyed by their inevitable coupling to the uncontrolled environment, which presents a major obstacle to quantum computation [1]. A practical quantum computer ultimately calls for operations on logical qubits protected by quantum error correction (QEC) [2–5] against unwanted errors with hopefully long enough coherence time. Therefore, to realize such a logical qubit with a longer coherence time than its individual physical components is considered as one of the most challenging goals for current quantum information processing [6]. For QEC, fragile quantum information needs first to be redundantly encoded in a logical subspace of a large Hilbert space [4]. Error syndromes that can distinguish the code space from other orthogonal error subspaces need to be monitored repetitively without perturbing the encoded information. Based on quantum non-demolition (QND) syndrome measurements, unitary recovery gates are adaptively applied to restore the original encoded information. To protect with QEC and to realize universal unitary manipulations of the logical qubit within the code space are necessary steps towards a practical quantum computer. The next stage is to demonstrate gate operations on the logical qubit under continuous QEC protection.

For previous logical qubit schemes based on multiple physical qubits [7–16], it is technically challenging to realize QEC and logical operations, because the number of error channels increases with the number of qubits and it also requires non-local gates on a collection of physical qubits for logical operations. Recently, a different encoding architecture based on a single bosonic oscillator (e.g. a microwave cavity mode) was proposed [17, 18] and has attracted a lot of interest [19–26]. In particular, QEC protection exceeding the break-even point has been demonstrated with a cat-code encoding [22] and gate operations on such logical qubits alone have been demonstrated without any QEC protection [24]. Taking advantage of the infinite dimensional Hilbert space of a harmonic oscillator, quantum information can be encoded with a single degree of

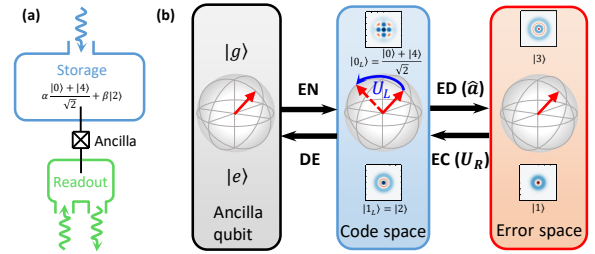


FIG. 1. Schematic of the experiments on binomial quantum code.

(a) The experimental device consists of a storage cavity as an oscillator for logical quantum state encoding, an ancillary transmon qubit facilitating all quantum operations, and a readout cavity for the ancilla measurement. The quantum states are encoded in the oscillator with the binomial code bases $|0_L\rangle = (|0\rangle + |4\rangle)/\sqrt{2}$ and $|1_L\rangle = |2\rangle$. (b) Operations on a single logical qubit. The quantum state of the ancilla qubit $\{|g\rangle, |e\rangle\}$ can be encoded (EN) to and decoded (DE) from the code space of the oscillator. A single photon loss changes the code space with even parity to the error space $\{|3\rangle, |1\rangle\}$ with odd parity. A high-fidelity and QND parity measurement can detect this error event, while leaving encoded quantum information untouched. Once a loss error is detected (ED), a unitary error correction (EC) recovery gate U_R can convert the error space back to the original code space. If there is no parity jump detected, the deterministic evolution of the code word can be corrected by another unitary recovery gate (not shown), completing a closed-loop QEC on the logical qubit. With the assistance of the ancilla, high-fidelity gate operations U_L on the logic qubit can also be implemented within the code space.

freedom. Most importantly, photon loss remains the dominant error channel, therefore there is still only one error syndrome that needs to be monitored. In addition, universal operations on the oscillator can be realized by dispersively coupling to a single ancilla transmon qubit, which allows fast and high-fidelity operations [27]. As a result, the requirements on hardware are greatly reduced [17, 18].

Besides the above advantages, a binomial code in a microwave cavity [28] is preferable because it has exact orthonormality of the code words and an explicit unitary operation for repumping photons into the photonic mode. The binomial code can exactly correct errors that are polynomial up to a specific order in photon creation and annihilation operators, including amplitude damping and displacement noise. Recently a controlled-NOT gate on a target qubit based on the lowest-order binomial code without QEC protection has been realized [26]. Here, we also choose the lowest-order binomial code that can be protected against a single photon loss error, and demonstrate full control on a single bosonic logical qubit with a repetitive QEC and a high-fidelity (97.0% process fidelity on average) universal gate set. The protected logical qubit has shown 2.8 times longer lifetime than the uncorrected one, and approaches the break-even point. The demonstrated complete logical qubit operations could be the foundations for developing fault-tolerant quantum computing [6, 29] and one-way quantum repeaters [30]. Additionally, we demonstrate for the first time a Ramsey experiment on the QEC protected logical qubit that shows two times longer coherence than the unprotected one, paving the way towards QEC enhanced quantum metrology [31].

The bosonic logical qubit experiment is implemented on a circuit quantum electrodynamics (cQED) architecture [32, 33] with a transmon qubit dispersively coupled to two three-dimensional (3D) cavities [19, 20, 22, 27, 33, 34], which is illustrated schematically in Fig. 1a. The ancilla qubit has an energy relaxation time $T_1 = 30 \mu\text{s}$ and a pure dephasing time $T_\phi = 120 \mu\text{s}$. The storage cavity serving as an oscillator (henceforth referred as the ‘‘oscillator’’) for encoding logical quantum states has a single-photon lifetime $\tau_s = 143 \mu\text{s}$ and a coherence time $252 \mu\text{s}$. Utilizing the large Hilbert space of the harmonic oscillator, the binomial code is constructed by superposing Fock states with binomial coefficients [28]. In our experiment, we choose the lowest-order binomial code with the code words

$$|0_L\rangle = (|0\rangle + |4\rangle)/\sqrt{2}, \quad (1)$$

$$|1_L\rangle = |2\rangle, \quad (2)$$

as shown in Fig. 1b. Both bases have the same average photon number of two as required by the QEC criteria [1]. This code can protect quantum information from one photon loss error, which is the dominant error in the microwave oscillator. A single photon loss delivers the logical states from the code space with even parity to an error space with odd parity, i.e. $\hat{a}|0_L\rangle = |3\rangle$ and $\hat{a}|1_L\rangle = |1\rangle$, where \hat{a} is the photon annihilation operator of the oscillator.

A complete set of operations on the bosonic logical qubit is illustrated in Fig. 1b. Besides serving as an ancilla for the error syndrome detection of the logical qubit, the transmon qubit provides the necessary non-linearity for implementing the quantum encoding, decoding, and error correcting recovery operation (U_R), as well as the universal single logical qubit operations in the binomial code space (logical gates

U_L). Through a sequence of control pulses on the system, all these operations on the logical qubit are realized based on the dispersive interaction between the ancilla and the oscillator [22, 35]

$$H_{\text{int}} = -\chi_{\text{qs}}\hat{a}^\dagger\hat{a}|e\rangle\langle e| - \frac{K}{2}\hat{a}^{\dagger 2}\hat{a}^2, \quad (3)$$

where $|e\rangle$ is the excited state of the ancilla qubit ($|g\rangle$ is the ground state), $\chi_{\text{qs}}/2\pi = 1.90$ MHz is the dispersive interaction strength, and $K/2\pi = 4.2$ kHz is the self-Kerr coefficient of the oscillator. The control pulses are synchronized and generated by field programmable gate arrays (FPGA) with homemade logics, and allow for fast real-time feedback control of the logical qubit (see Supplementary Materials for the experimental apparatus). Specially, the pulse shapes are numerically optimized with the gradient ascent pulse engineering (GRAPE) method [36, 37] based on carefully calibrated experimental parameters.

First, we demonstrate the encoding and decoding process, where quantum information is transferred between the ancilla qubit $\{|g\rangle, |e\rangle\}$ and the binomial code space $\{|0_L\rangle, |1_L\rangle\}$ of the oscillator. Process tomography [1] is used to benchmark our encoding and decoding performance, and the fidelity is defined as $F_\chi = \text{tr}(\chi_M\chi_{\text{ideal}})$, with χ_M (χ_{ideal}) being the derived 4×4 process matrix for experimental (ideal) operation (see Methods). Figure 2a shows the χ_M for a sequential encoding and decoding process ($\chi_{\text{ideal}} = \mathbb{I}$) and indicates a fidelity of 93.1%.

The quantum information in the binomial code space can be protected from a single photon loss by the QEC process (including both error detection and correction). A photon number parity measurement can distinguish the code and error spaces (Fig. 1b) without perturbing the encoded information [20], and thus serves as the error syndrome for error detection. Once a parity change is detected, the state in the error space can be converted back to the original code space by a unitary recovery gate U_R . As opposed to the cat code, where corrections can be performed at the end of error-syndrome tracking [22], the photon loss error in our experiment needs to be corrected immediately since this particular binomial code does not tolerate two or more photon losses. Repeated such processes can therefore protect the information stored in the logical qubit. However, a trade-off needs to be considered between more frequent parity measurement to avoid missing photon loss errors and finite detection and recovery fidelities causing extra information loss.

The experimental protocol of repetitive QEC is shown in Fig. 2a, where a two-layer QEC procedure is adapted to balance the operation and photon loss errors. The top-layer QEC consists of several bottom-layer QEC steps, and each step corrects photon loss error but tolerates the backaction from the detection of no parity jump until the last step. Therefore, the top-layer QEC recovers the quantum information in code space and is repeated many times, while the bottom-layer QEC conserves parity in a deformed code space. The optimal scheme for current experiments consists of two bottom-

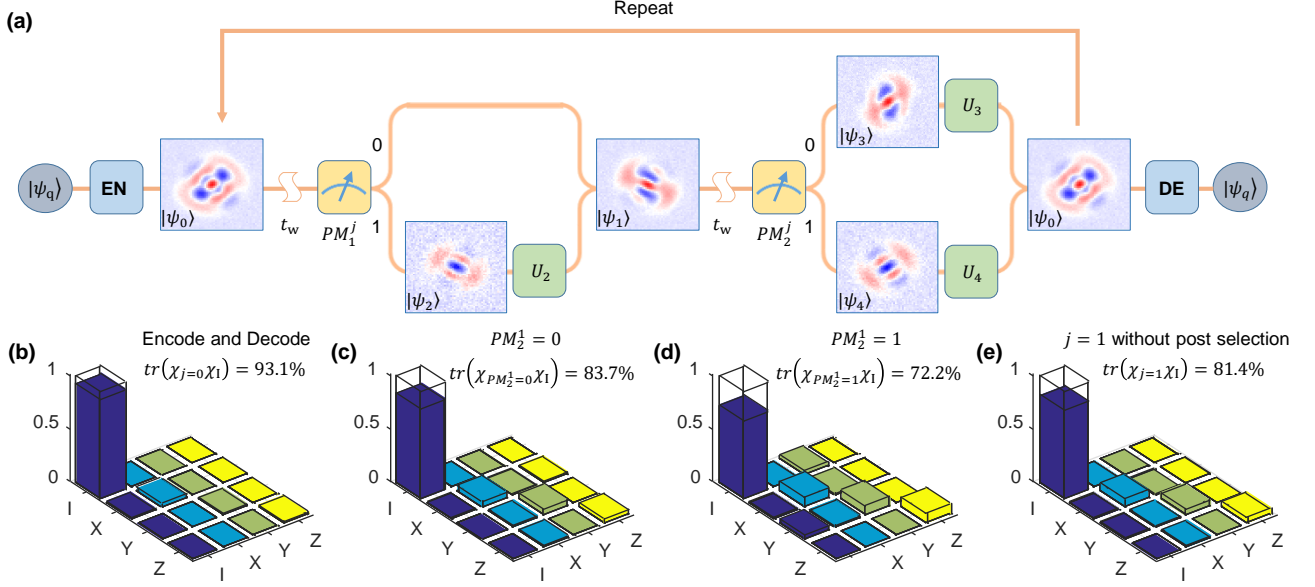


FIG. 2. Protocol of the repetitive QEC and process tomography. (a) The experimental procedure. The experiment begins with encoding an arbitrary superposition state $|\psi_q\rangle = \alpha|g\rangle + \beta|e\rangle$ of the ancilla qubit onto the oscillator state $|\psi_0\rangle = \alpha(|0\rangle + |4\rangle)/\sqrt{2} + \beta|2\rangle$ (process EN). After a waiting time $t_w \approx 17.9 \mu\text{s}$, a parity measurement is performed. $PM_1^j = 0$ (the 1st parity measurement of the j^{th} round) indicates that no photon loss error occurs (two or more photon loss errors can not be distinguished but have a small probability), and the state of the oscillator undergoes a deterministic evolution to a deformed code space as $|\psi_1\rangle = \alpha(\cos\theta_1|0\rangle + \sin\theta_1 e^{i\varphi_4}|4\rangle)/\sqrt{2} + \beta e^{i\varphi_2}|2\rangle$, and no correction action is applied. $PM_1^j = 1$ indicates that one photon loss error occurs, and the oscillator state becomes $|\psi_2\rangle = \alpha e^{i\varphi_3}|3\rangle + \beta|1\rangle$. A π pulse is first applied to flip the ancilla qubit to the $|g\rangle$ state to minimize the detrimental effect from the ancilla qubit decoherence, and then a unitary recovery gate U_2 is applied immediately to convert $|\psi_2\rangle$ to $|\psi_1\rangle$. Note that after another waiting time t_w , a second parity measurement is performed. Similarly, $PM_2^j = 0$ or 1 indicate no or one photon loss occurs, and the oscillator state becomes $|\psi_3\rangle = \alpha(\cos\theta_2|0\rangle + \sin\theta_2 e^{i\varphi_4}|4\rangle)/\sqrt{2} + \beta e^{i\varphi_2}|2\rangle$ and $|\psi_4\rangle = \alpha e^{i\varphi_3}|3\rangle + \beta|1\rangle$, respectively. Unitary gates U_3 and U_4 are then applied correspondingly to restore the original state $|\psi_0\rangle$. This error correction process is repeated 1 – 19 times followed by a decoding process (DE) to the ancilla qubit. $|\psi_{0-4}\rangle$ are all measured Wigner functions for $\alpha = 1/\sqrt{2}$ and $\beta = -i/\sqrt{2}$. (b-e) χ matrices of the process tomography, with (b) for encoding followed immediately by the decoding process, (c)&(d) for one round of error correction for $PM_2^j = 0$ (with probability 79.3%) and $PM_2^j = 1$ (with probability 20.7%), respectively, (e) for one round of correction without post-selecting $PM_2^j = 0$ or 1. Here, only the real parts are shown while the imaginary parts are nearly zero.

layer QEC steps with a waiting time $t_w = 17.9 \mu\text{s}$. The outcome of first error detection $PM = 0$ indicates that no photon loss error occurs and the state of the oscillator undergoes an evolution from $|\psi_0\rangle = \alpha|0_L\rangle + \beta|0_L\rangle$ to $|\psi_1\rangle = \alpha|0'_L\rangle + \beta|1'_L\rangle$, with a deformation of code space bases $|0'_L\rangle = (\cos\theta_1|0\rangle + \sin\theta_1 e^{i\varphi_4}|4\rangle)/\sqrt{2}$ and $|1'_L\rangle = e^{i\varphi_2}|2\rangle$. We note that the above unitary evolution is only an approximation to the non-unitary backaction associated with the no-parity-jump evolution $e^{-(\kappa/2)\hat{a}^\dagger \hat{a} t}$ valid to first order in κt_w [28]. It is also worth noting that no detected parity change can not rule out the possibility of having two-photon losses ($\sim 2.1\%$), which causes complete quantum information loss. For $PM = 1$, one photon loss error occurs (the probability of having a three-photon loss $\sim 0.14\%$ can be neglected), and the oscillator state becomes $|\psi_2\rangle = \alpha e^{i\varphi_3}|3\rangle + \beta|1\rangle$ and a unitary recovery gate U_2 has to be applied immediately to convert $|\psi_2\rangle$ to $|\psi_1\rangle$ in the deformed code space. After an additional waiting time t_w , another error detection is performed for the second bottom-layer QEC step. Similarly, $PM = 0$ and 1 indicate a further deformation of code space to $|\psi_3\rangle$ and a jump to error space with

$|\psi_4\rangle = \alpha e^{i\varphi_3}|3\rangle + \beta|1\rangle$, respectively. Then, unitary gates U_3 and U_4 are applied correspondingly to restore the original state $|\psi_0\rangle$, completing one round of top-layer error correction. In Figs. 2c-e, the process matrices are presented for the process after the second error detection in the first round of top-layer QEC, showing a good fidelity of 81.4%.

Figure 3a shows the process fidelity $F_\chi(t)$ with the repetitive QEC (green) decaying exponentially as a function of time, where the two-layer error correction process is repeated $j = 1 - 19$ times. For comparison, the process fidelities of the uncorrected binomial quantum code (red), the uncorrected transmon qubit (black), and the uncorrected Fock $\{|0\rangle, |1\rangle\}$ encoding of the oscillator (blue) are also plotted. All curves are fitted using $F_\chi(t) = 0.25 + Ae^{-t/\tau}$, where τ is the lifetime. τ of the corrected binomial code is 5.3 times longer than the uncorrected transmon qubit, 2.8 times longer than the uncorrected binomial code, and only less than 8% lower than the uncorrected Fock encoding that defines the break-even point for the QEC [22]. These results demonstrate that the experimental system and scheme are robust and can indeed protect the encoded bosonic code from the photon loss error.

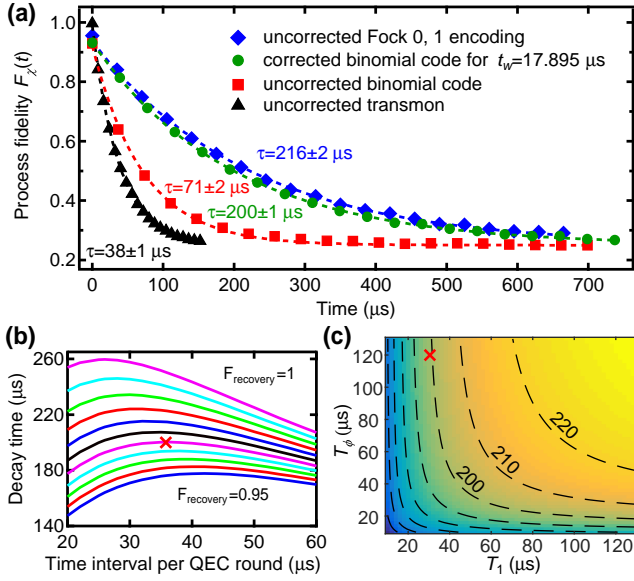


FIG. 3. **QEC performance.** (a) Green: Process fidelity $F_\chi(t)$ with the repetitive QEC decays exponentially as a function of time. Each point is obtained by 40,000 averages and the error bars are smaller than marker sizes. For comparison, the process fidelity decay curves of the uncorrected binomial quantum code (red), the uncorrected transmon qubit (black), and the uncorrected Fock $\{|0\rangle, |1\rangle\}$ encoding (blue) are also plotted. All curves are fit using $F_\chi(t) = 0.25 + Ae^{-t/\tau}$ (dotted lines). (b) Theoretically expected process fidelity decay time for the protocol in Fig. 2a with the measured parameters but with different recovery gate fidelities (the colored lines correspond to fidelities from 0.95 to 1 with a step of 0.005). The cross indicates our experimental result, implying a recovery gate fidelity of about 97.0%. (c) Expected process fidelity decay time as a function of T_1 and T_ϕ . Dashed lines represent isolines from 150 μs to 220 μs with a step of 10 μs . The cross indicates our experimental result. In order to extend the logical qubit lifetime beyond that of Fock state $\{|0\rangle, |1\rangle\}$ encoding, T_1 needs to be doubled while T_ϕ remains the same.

The experiment is mainly limited by the decoherence of the ancilla qubit that induces imperfections and deserves further investigation. Since the ancilla facilitates both error detection and gate operations, the ancilla decoherence induces errors for these processes and prevents more frequent QEC. On the other hand, with a larger interval between QECs, there is a higher probability of having undetectable two-photon losses and a larger dephasing effect induced by photon losses due to the non-commutativity of the annihilation operation \hat{a} and the self-Kerr term $\frac{\kappa}{2}\hat{a}^{\dagger 2}\hat{a}^2$ (see Supplementary Materials). To illustrate this trade-off relation, Fig. 3b shows the numerically predicted decay time as a function of the tracking interval per two error detections following the protocol in Fig. 2a. It predicts a shorter optimal t_w and a longer decay time for a higher recovery gate fidelity. Our experimental result is indicated by the cross, implying a recovery gate fidelity of about 97.0% that is mainly limited by the qubit decoherence during the recovery gates. In order to extend the logical qubit life time beyond that of Fock state $\{|0\rangle, |1\rangle\}$ encoding, either a better strategy with at least four bottom-layer QEC steps needs to

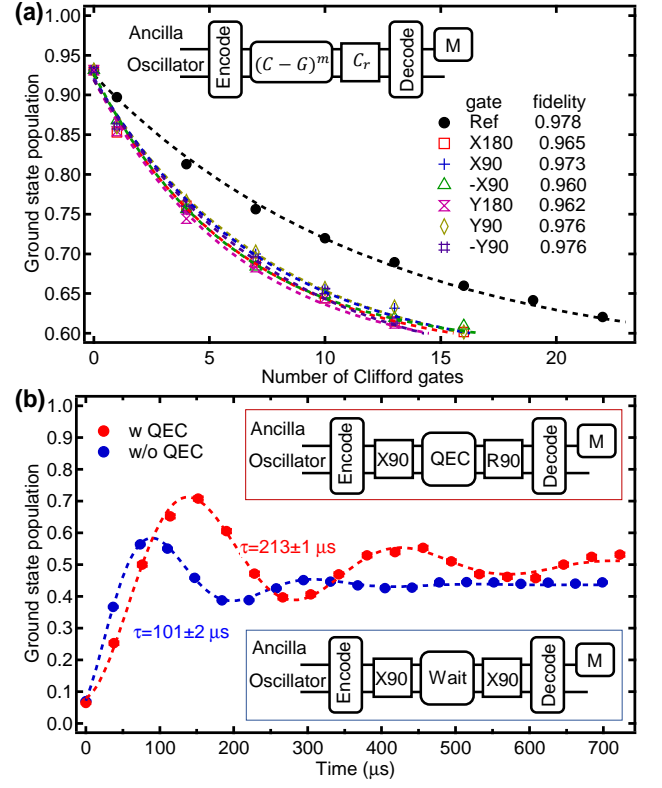


FIG. 4. **Gate operations on the logical qubit and Ramsey interferometry on the QEC protected logical qubit.** (a) Randomized benchmarking is used to quantify the gate performance on the logical qubit, with the protocol shown in the inset. All experiments start with an encoding and end with a decoding followed by ancilla qubit measurement. The reference curve is measured after applying sequences of m random Clifford gates, while the $\pm X90, \pm Y90, X180, Y180$ ($\pm\pi/2$ rotation along x - or y -axis, and π rotation along x - or y -axis, respectively) curves are realized after applying sequences that interleave the corresponding gate with m random Clifford gates. Each sequence is followed by a recovery Clifford gate in the end right before the final measurement. The number of random sequences for each length m in our experiment is $k = 100$ and each random sequence is repeated over 5,000 times. All curves are fitted by $F_{\text{RB}} = Ap^m + B$ with different sequence decay p . The reference decay indicates the average error of the single-qubit gates, while the ratio of the interleaved and reference decay gives the specific gate fidelity. The averaged single-qubit gate error $r_{\text{gate}} \sim 0.031$. (b) Ramsey interferometry of logical qubit, with insets showing the experimental sequences. The Ramsey oscillation on the QEC protected logical qubit (red) gives a coherence time twice longer than that without QEC protection (blue), demonstrating a real gain of the coherence from QEC. For the process without QEC, the intervals between gates are chosen such that the Kerr rotations of $|4\rangle$ are integer multiples of 2π . The rotation axis of the second $\pi/2$ gate is fixed and the oscillation comes from the Kerr rotation of $|2\rangle$. The population converges to a value slightly lower than 0.5, which comes from the leakage out of the computational space during the long process without protection. For the QEC protected case, the rotation axis of the second $\pi/2$ gate (R90) varies in the x - y plane with an interval of $\pi/4$.

be implemented with current qubit coherence (but demanding more adaptive gate calibrations, see Supplementary Materials), or the coherence time of the ancilla qubit needs to be improved. As depicted in Fig. 3c, this goal can be achieved if we can double T_1 while keep the same T_ϕ . By comparison, a cat code does not have this recovery gate error issue, and instead only requires tracking the number of errors and a correction at the end of the whole QEC process [22]. If the recovery gate itself is perfect and we only have detection errors, we in principle can achieve a decay time after QEC over 260 μs , more than 20% longer than for Fock state $\{|0\rangle, |1\rangle\}$ encoding.

To fully exploit the binomial encoding for future quantum information processing, gate operations on the logical qubits are indispensable. Thanks to the single bosonic oscillator encoding, we are able to implement the logical qubit gates by a universal control of the state of the oscillator, instead of encoding/decoding to the ancilla qubit. A randomized benchmarking experiment [38–41] is performed to determine the fidelity of the Clifford gates on the logical qubit. Figure 4a shows the results with an averaged gate error $r_{\text{gate}} \sim 0.031$. These gates fidelities could be improved further by a more careful calibration of the GRAPE pulses. We note that the T gate does not belong to the Clifford group, so it can not be characterized by randomized benchmarking. We instead perform repeated gates to extract the gate fidelity of about 98.7% (data shown in the Supplementary Materials).

With the QEC and the high-fidelity universal operation of the logical qubit in hand, we demonstrate a Ramsey experiment on the QEC protected logical qubit that indeed shows longer coherence. Figure 4b insets show the experimental sequences for the logical qubit Ramsey experiments with and without QEC, and both experiments also combine an encoding and decoding process. The results are fitted with an exponentially damped sinusoidal function. The Ramsey experiment performed on the logical qubit without QEC gives a coherence time of 101 μs . The interference fringes against the evolution time correspond to a Kerr nonlinearity induced phase change of the logical qubit. It is worth noting that the self-Kerr does not cause errors in the lowest-order binomial code in the absence of cavity photon decay. A particular frame can be chosen to match the rotation of $|4\rangle$ relative to $|0\rangle$ so that $|0\rangle$ and $|4\rangle$ are degenerate, while $|2\rangle$ has a slightly different frequency. However, the resulting phase rotation of the logical qubit is purely deterministic and thus there is no decoherence associated with the self-Kerr effect. This is true even if the higher-order corrections to Kerr nonlinearity are taken into account, which is one of the nice features of the lowest-order binomial code.

For comparison, the experiment on the QEC protected logical qubit gives a twice longer coherence time of 213 μs , demonstrating a real gain of the coherence from QEC. The Ramsey oscillation in this QEC protected case comes from the variable rotation axis of the second $\pi/2$ gate. Since the Ramsey interferometry has been widely used for precision measurements, our results represent an important advance towards QEC enhanced metrology based on logical qubits.

In summary, we have demonstrated a real-time repetitive QEC and universal gate set on a bosonic logical qubit in a superconducting circuit. Our experiment shows that the binomial encoding in a 3D cQED architecture is hardware-efficient for QEC and logical operations and represents a promising platform towards future quantum algorithms based on multiple logical qubits with QEC protection. Our work provides a starting point for future works: realize logical qubit with binomial code, generalize the tools realized in this work to multiple oscillators (logical qubits), and realize fault-tolerant error detection, correction, as well as logical gates. Current experimental techniques are feasible to realize more logical qubits by integrating more cavities or modes in a compact 3D structure [42]. Our results motivate further investigations of the superconducting quantum processor and envision the route towards fault-tolerant implementation of QEC and gates based on bosonic encoding [6, 29].

* These two authors contributed equally to this work.

† clzou321@ustc.edu.cn

‡ luyansun@tsinghua.edu.cn

- [1] M. A. Nielsen and I. L. Chuang, *Quantum Computation and Quantum Information* (Cambridge Univ. Press, 2000).
- [2] P. W. Shor, "Scheme for reducing decoherence in quantum computer memory," *Phys. Rev. A* **52**, 2493 (1995).
- [3] A. Steane, "Multiple particle interference and quantum error correction," *Proc. Roy. Soc. Lond. A* **452**, 2551 (1996).
- [4] D. Gottesman, "An introduction to quantum error correction and fault-tolerant quantum computation," *Proceeding of Symposia in Applied Mathematics* **68**, 13 (2010).
- [5] A. G. Fowler, M. Mariantoni, J. M. Martinis, and A. N. Cleland, "Surface codes: Towards practical large-scale quantum computation," *Phys. Rev. A* **86**, 032324 (2012).
- [6] M. H. Devoret and R. J. Schoelkopf, "Superconducting circuits for quantum information: an outlook." *Science* **339**, 1169 (2013).
- [7] D. G. Cory, M. Price, W. Maas, E. Knill, R. Laflamme, W. H. Zurek, T. F. Havel, and S. Somaroo, "Experimental quantum error correction," *Phys. Rev. Lett.* **81**, 2152 (1998).
- [8] J. Chiaverini, D. Leibfried, T. Schaetz, M. D. Barrett, R. B. Blakestad, J. Britton, W. M. Itano, J. D. Jost, E. Knill, C. Langer, R. Ozeri, and D. J. Wineland, "Realization of quantum error correction," *Nature* **432**, 602 (2004).
- [9] P. Schindler, J. T. Barreiro, T. Monz, V. Nebendahl, D. Nigg, M. Chwalla, M. Hennrich, and R. Blatt, "Experimental Repetitive Quantum Error Correction," *Science* **332**, 1059 (2011).
- [10] M. D. Reed, L. DiCarlo, S. E. Nigg, L. Sun, L. Frunzio, S. M. Girvin, and R. J. Schoelkopf, "Realization of three-qubit quantum error correction with superconducting circuits," *Nature* **482**, 382 (2012).
- [11] G. Waldherr, Y. Wang, S. Zaiser, M. Jamali, T. Schulte-Herbrüggen, H. Abe, T. Ohshima, J. Isoya, J. F. Du, P. Neumann, and J. Wrachtrup, "Quantum error correction in a solid-state hybrid spin register." *Nature* **506**, 204 (2014).
- [12] T. H. Taminiau, J. Cramer, T. van der Sar, V. V. Dobrovitski, and R. Hanson, "Universal control and error correction in multi-qubit spin registers in diamond." *Nat. Nanotechnol.* **9**, 171 (2014).

- [13] J. Cramer, N. Kalb, M. A. Rol, B. Hensen, M. S. Blok, M. Markham, D. J. Twitchen, R. Hanson, and T. H. Taminiou, “Repeated quantum error correction on a continuously encoded qubit by real-time feedback,” *Nat. Commun.* **7**, 11526 (2016).
- [14] J. Kelly, R. Barends, A. G. Fowler, A. Megrant, E. Jeffrey, T. C. White, D. Sank, J. Y. Mutus, B. Campbell, Y. Chen, Z. Chen, B. Chiaro, A. Dunsworth, I.-C. Hoi, C. Neill, P. J. J. O’Malley, C. Quintana, P. Roushan, A. Vainsencher, J. Wenner, A. N. Cleland, and J. M. Martinis, “State preservation by repetitive error detection in a superconducting quantum circuit,” *Nature* **519**, 66 (2015).
- [15] A. D. Córcoles, E. Magesan, S. J. Srinivasan, A. W. Cross, M. Steffen, J. M. Gambetta, and J. M. Chow, “Demonstration of a quantum error detection code using a square lattice of four superconducting qubits,” *Nature Communications* **6**, 6979 (2015).
- [16] D. Ristè, S. Poletto, M.-Z. Huang, A. Bruno, V. Vesterinen, O.-P. Saira, and L. DiCarlo, “Detecting bit-flip errors in a logical qubit using stabilizer measurements,” *Nat. Commun.* **6**, 6983 (2015).
- [17] Z. Leghtas, G. Kirchmair, B. Vlastakis, R. J. Schoelkopf, M. H. Devoret, and M. Mirrahimi, “Hardware-Efficient Autonomous Quantum Memory Protection,” *Phys. Rev. Lett.* **111**, 120501 (2013).
- [18] M. Mirrahimi, Z. Leghtas, V. V. Albert, S. Touzard, R. J. Schoelkopf, L. Jiang, and M. H. Devoret, “Dynamically protected cat-qubits: a new paradigm for universal quantum computation,” *New J. Phys.* **16**, 045014 (2014).
- [19] B. Vlastakis, G. Kirchmair, Z. Leghtas, S. E. Nigg, L. Frunzio, S. M. Girvin, M. Mirrahimi, M. H. Devoret, and R. J. Schoelkopf, “Deterministically encoding quantum information using 100-photon Schrödinger cat states,” *Science* **342**, 607 (2013).
- [20] L. Sun, A. Petrenko, Z. Leghtas, B. Vlastakis, G. Kirchmair, K. M. Sliwa, A. Narla, M. Hatridge, S. Shankar, J. Blumoff, L. Frunzio, M. Mirrahimi, M. H. Devoret, and R. J. Schoelkopf, “Tracking photon jumps with repeated quantum non-demolition parity measurements,” *Nature* **511**, 444 (2014).
- [21] Z. Leghtas, S. Touzard, I. M. Pop, A. Kou, B. Vlastakis, A. Petrenko, K. M. Sliwa, A. Narla, S. Shankar, M. J. Hatridge, M. Reagor, L. Frunzio, R. J. Schoelkopf, M. Mirrahimi, and M. H. Devoret, “Confining the state of light to a quantum manifold by engineered two-photon loss,” *Science* **347**, 853 (2015).
- [22] N. Ofek, A. Petrenko, R. Heeres, P. Reinhold, Z. Leghtas, B. Vlastakis, Y. Liu, L. Frunzio, S. M. Girvin, L. Jiang, M. Mirrahimi, M. H. Devoret, and R. J. Schoelkopf, “Extending the lifetime of a quantum bit with error correction in superconducting circuits,” *Nature* **536**, 441 (2016).
- [23] C. Wang, Y. Y. Gao, P. Reinhold, R. W. Heeres, N. Ofek, K. Chou, C. Axline, M. Reagor, J. Blumoff, K. M. Sliwa, L. Frunzio, S. M. Girvin, L. Jiang, M. Mirrahimi, M. H. Devoret, and R. J. Schoelkopf, “A Schrodinger cat living in two boxes,” *Science* **352**, 1087 (2016).
- [24] R. W. Heeres, P. Reinhold, N. Ofek, L. Frunzio, L. Jiang, M. H. Devoret, and R. J. Schoelkopf, “Implementing a universal gate set on a logical qubit encoded in an oscillator,” *Nat. Commun.* **8**, 94 (2017).
- [25] K. S. Chou, J. Z. Blumoff, C. S. Wang, P. C. Reinhold, C. J. Axline, Y. Y. Gao, L. Frunzio, M. H. Devoret, L. Jiang, and R. J. Schoelkopf, “Deterministic teleportation of a quantum gate between two logical qubits,” *arXiv*, 1801.05283 (2018).
- [26] S. Rosenblum, Y. Y. Gao, P. Reinhold, C. Wang, C. J. Axline, L. Frunzio, S. M. Girvin, L. Jiang, M. Mirrahimi, M. H. Devoret, and R. J. Schoelkopf, “A CNOT gate between multi-photon qubits encoded in two cavities,” *Nat. Commun.* **9**, 652 (2018).
- [27] S. Krastanov, V. V. Albert, C. Shen, C.-L. Zou, R. W. Heeres, B. Vlastakis, R. J. Schoelkopf, and L. Jiang, “Universal control of an oscillator with dispersive coupling to a qubit,” *Phys. Rev. A* **92**, 040303 (2015).
- [28] M. H. Michael, M. Silveri, R. T. Brierley, V. V. Albert, J. Salmilehto, L. Jiang, and S. M. Girvin, “New Class of Quantum Error-Correcting Codes for a Bosonic Mode,” *Phys. Rev. X* **6**, 031006 (2016).
- [29] S. Rosenblum, P. Reinhold, M. Mirrahimi, L. Jiang, L. Frunzio, and R. Schoelkopf, “Fault-tolerant measurement of a quantum error syndrome,” *arXiv:1803.00102* (2018).
- [30] L. Li, C.-L. Zou, V. V. Albert, S. Muralidharan, S. M. Girvin, and L. Jiang, “Cat Codes with Optimal Decoherence Suppression for a Lossy Bosonic Channel,” *Phys. Rev. Lett.* **119**, 030502 (2017).
- [31] S. Zhou, M. Zhang, J. Preskill, and L. Jiang, “Achieving the Heisenberg limit in quantum metrology using quantum error correction,” *Nat. Commun.* **9**, 78 (2018).
- [32] A. Wallraff, D. I. Schuster, A. Blais, L. Frunzio, R.-S. Huang, J. Majer, S. Kumar, S. M. Girvin, and R. J. Schoelkopf, “Strong coupling of a single photon to a superconducting qubit using circuit quantum electrodynamics,” *Nature* **431**, 162 (2004).
- [33] H. Paik, D. I. Schuster, L. S. Bishop, G. Kirchmair, G. Catelani, a. P. Sears, B. R. Johnson, M. J. Reagor, L. Frunzio, L. I. Glazman, S. M. Girvin, M. H. Devoret, and R. J. Schoelkopf, “Observation of High Coherence in Josephson Junction Qubits Measured in a Three-Dimensional Circuit QED Architecture,” *Phys. Rev. Lett.* **107**, 240501 (2011).
- [34] K. Liu, Y. Xu, W. Wang, S.-B. Zheng, T. Roy, S. Kundu, M. Chand, A. Ranadive, R. Vijay, Y. Song, L. Duan, and L. Sun, “A twofold quantum delayed-choice experiment in a superconducting circuit,” *Sci. Adv.* **3**, e1603159 (2017).
- [35] G. Kirchmair, B. Vlastakis, Z. Leghtas, S. E. Nigg, H. Paik, E. Ginossar, M. Mirrahimi, L. Frunzio, S. M. Girvin, and R. J. Schoelkopf, “Observation of quantum state collapse and revival due to the single-photon Kerr effect,” *Nature* **495**, 205 (2013).
- [36] N. Khaneja, T. Reiss, C. Kehlet, T. Schulte-Herbrüggen, and S. J. Glaser, “Optimal control of coupled spin dynamics: design of nmr pulse sequences by gradient ascent algorithms,” *Journal of magnetic resonance* **172**, 296 (2005).
- [37] P. De Fouquieres, S. Schirmer, S. Glaser, and I. Kuprov, “Second order gradient ascent pulse engineering,” *Journal of Magnetic Resonance* **212**, 412 (2011).
- [38] R. Barends, J. Kelly, A. Megrant, A. Veitia, D. Sank, E. Jeffrey, T. C. White, J. Mutus, a. G. Fowler, B. Campbell, Y. Chen, Z. Chen, B. Chiaro, A. Dunsworth, C. Neill, P. O’Malley, P. Roushan, A. Vainsencher, J. Wenner, a. N. Korotkov, a. N. Cleland, and J. M. Martinis, “Superconducting quantum circuits at the surface code threshold for fault tolerance,” *Nature* **508**, 500 (2014).
- [39] E. Knill, D. Leibfried, R. Reichle, J. Britton, R. B. Blakestad, J. D. Jost, C. Langer, R. Ozeri, S. Seidelin, and D. J. Wineland, “Randomized benchmarking of quantum gates,” *Phys. Rev. A* **77**, 012307 (2008).
- [40] C. A. Ryan, M. Laforest, and R. Laflamme, “Randomized benchmarking of single- and multi-qubit control in liquid-state nmr quantum information processing,” *New J. Phys.* **11**, 013034 (2009).
- [41] E. Magesan, J. M. Gambetta, B. R. Johnson, C. A. Ryan, J. M. Chow, S. T. Merkel, M. P. da Silva, G. A. Keefe, M. B. Rothwell, T. A. Ohki, M. B. Ketchen, and M. Steffen, “Efficient measurement of quantum gate error by interleaved randomized

- benchmarking,” *Phys. Rev. Lett.* **109**, 080505 (2012).
- [42] C. Axline, M. Reagor, R. Heeres, P. Reinhold, C. Wang, K. Shain, W. Pfaff, Y. Chu, L. Frunzio, and R. J. Schoelkopf, “An architecture for integrating planar and 3D cQED devices,” *Appl. Phys. Lett.* **109**, 042601 (2016).
- [43] M. Hatridge, R. Vijay, D. H. Slichter, J. Clarke, and I. Siddiqi, “Dispersive magnetometry with a quantum limited SQUID parametric amplifier,” *Phys. Rev. B* **83**, 134501 (2011).
- [44] T. Roy, S. Kundu, M. Chand, A. M. Vadiraj, A. Ranadive, N. Nehra, M. P. Patankar, J. Aumentado, A. A. Clerk, and R. Vijay, “Broadband parametric amplification with impedance engineering: Beyond the gain-bandwidth product,” *Appl. Phys. Lett.* **107**, 262601 (2015).
- [45] A. Kamal, A. Marblestone, and M. H. Devoret, “Signal-to-pump back action and self-oscillation in double-pump Josephson parametric amplifier,” *Phys. Rev. B* **79**, 184301 (2009).
- [46] K. W. Murch, S. J. Weber, C. Macklin, and I. Siddiqi, “Observing single quantum trajectories of a superconducting quantum bit,” *Nature* **502**, 211 (2013).
- [47] J. M. Chow, J. M. Gambetta, L. Tornberg, J. Koch, L. S. Bishop, A. A. Houck, B. R. Johnson, L. Frunzio, S. M. Girvin, and R. J. Schoelkopf, “Randomized Benchmarking and Process Tomography for Gate Errors in a Solid-State Qubit,” *Phys. Rev. Lett.* **102**, 090502 (2009).

Acknowledgments

We thank N. Ofek and Y. Liu for valuable suggestions on FPGA programming, L. Jiang, L. Li, and R. Schoelkopf for helpful discussions. LS acknowledges the support from National Natural Science Foundation of China Grant No.11474177, National Key Research and Development Program of China No.2017YFA0304303, and the Thousand Youth Fellowship program in China. SMG acknowledges grants from ARO W911NF1410011 and NSF DMR-1609326. LS also thanks R. Vijay and his group for help on the parametric amplifier measurements.

Author contributions

LH and LS developed the FPGA logic. LH and YM performed the experiment and analyzed the data with the assistance of WC, XM, YX, and WW. LS directed the experiment. LMD, CLZ, and LS proposed the experiment. CLZ, YW, SMG, and LMD provided theoretical support. WC fabricated the JPA. LH and XM fabricated the devices with the assistance of YX, HW, and YPS. CLZ, SMG, and LS wrote the manuscript with feedback from all authors.

Competing financial interests

The authors declare no competing financial interests.

Supplementary Information “Demonstration of quantum error correction and universal gate set on a binomial bosonic logical qubit”

L. Hu,^{1,*} Y. Ma,^{1,*} W. Cai,¹ X. Mu,¹ Y. Xu,¹ W. Wang,¹ Y. Wu,² H. Wang,¹
Y. P. Song,¹ C.-L. Zou,^{3,†} S. M. Girvin,⁴ L.-M. Duan,^{1,2} and L. Sun^{1,‡}

¹Center for Quantum Information, Institute for Interdisciplinary Information Sciences, Tsinghua University, Beijing 100084, China

²Department of Physics, University of Michigan, Ann Arbor, Michigan 48109, USA

³Key Laboratory of Quantum Information, CAS, University of Science and Technology of China, Hefei, Anhui 230026, P. R. China

⁴Departments of Applied Physics and Physics, Yale University, New Haven, CT 06511, USA

EXPERIMENTAL DEVICE AND SETUP

Our experimental device is measured in a dilution refrigerator with a base temperature about 10 mK. Details of the experimental setup are shown in Fig. S1a. The device has a transmon qubit (the ancilla) dispersively coupled to both a readout cavity and a storage cavity (the oscillator). The ancilla qubit is fabricated on a *c*-plane sapphire (Al₂O₃) substrate with a double-angle evaporation of aluminum after a single electron-beam lithography step. The cavities are made of high purity 5N5 aluminum and are chemically etched for a better coherence time [1, 2]. A Josephson parametric Amplifier (JPA) [3–6] is used as the first stage of amplification, allowing for a high-fidelity single-shot measurement of the qubit (see the section on the Readout Properties).

We follow a similar hardware setup and quantum control architecture strategy based on field programmable gate array (FPGA) boards as Dr. Schoelkopf’s lab at Yale University for our experiment [7]. The ancilla qubit, the oscillator, and the readout cavity are each controlled by a FPGA board. All three FPGA boards are X6-1000M from Innovative Integration in a VPXI-ePC chassis as shown in Fig. S1b. Each board integrates two digital-to-analog converters (DACs), two analog-to-digital converters (ADCs), 64 independent digital inputs/outputs (DIO), and a Xilinx VIRTEX-6 FPGA with customized logic for control. All FPGAs are loaded with the same logic, and we send different but synchronized instructions to each FPGA to realize the desired operations. A VPX-COMEX module is used to generate 1 GHz clocks (1 GHz sampling rate for all ADCs and DACs) and synchronized triggers for all three boards, so that all DIO, ADCs, and DACs on different boards are synchronized into one entirety. The down-converted returning readout signal from the device is fed into the ADCs of one FPGA board, within which the demodulation and calculations are performed and the results are discriminated into digitized signals. These final readout signals are not only sent to the host PC, but also distributed among all FPGAs through the DIO ports for inter-board communication. The latter is essential because the feedback operations coordinated among all three boards depend on the same digitized readout result. The total feedback latency, the time interval between receiving the last point of the readout signal and sending out the first point of the control signal, is 336 ns in our experiment. This time includes the signal travel time

Term	Measured (Predicted)
$\omega_q/2\pi$	5.692 GHz
$\omega_s/2\pi$	7.634 GHz
$\omega_r/2\pi$	8.610 GHz
$K_q/2\pi$	232 MHz
$K_r/2\pi$	(14.4 kHz)
$K_s/2\pi$	4.23 kHz
$K'_s/2\pi$	0.45 kHz
$\chi_{qs}/2\pi$	1.90 MHz
$\chi_{qr}/2\pi$	3.65 MHz
$\chi_{sr}/2\pi$	(15.6 kHz)

TABLE I. Hamiltonian parameters. The predicted values in parentheses are calculated according to $\chi_{pp'} = -2\sqrt{K_p K'_p}$ based on the black-box quantization theory [8].

	Ancilla	Oscillator	Readout
T_1	30 μ s	-	-
T_2	40 μ s	-	-
T_ϕ	120 μ s	-	-
$\tau_{s,r}(K_{s,r}/2\pi)$	-	143 μ s (1.1 kHz)	44 ns (3.62 MHz)
T_2^s	-	252 μ s	-
ground state	99.2%	99.4%	> 99.9%

TABLE II. Coherent times and thermal populations of the ancilla qubit, the oscillator, and the readout cavity.

through the experimental circuitry.

MEASURED SYSTEM PARAMETERS, COHERENCE TIMES, AND MEASUREMENT PROPERTIES

In the strong-dispersive regime, our system consisting of two cavities and one ancilla qubit can be described by the Hamiltonian

$$\begin{aligned} \hat{H}/\hbar = & \omega_q \hat{a}_q^\dagger \hat{a}_q + \omega_r \hat{a}_r^\dagger \hat{a}_r + \omega_s \hat{a}_s^\dagger \hat{a}_s \\ & - \chi_{qs} \hat{a}_q^\dagger \hat{a}_q \hat{a}_s^\dagger \hat{a}_s - \chi_{qr} \hat{a}_q^\dagger \hat{a}_q \hat{a}_r^\dagger \hat{a}_r - \chi_{sr} \hat{a}_s^\dagger \hat{a}_s \hat{a}_r^\dagger \hat{a}_r \\ & - \frac{K_q}{2} \hat{a}_q^{\dagger 2} \hat{a}_q^2 - \frac{K_r}{2} \hat{a}_r^{\dagger 2} \hat{a}_r^2 - \frac{K_s}{2} \hat{a}_s^{\dagger 2} \hat{a}_s^2 - \frac{K'_s}{6} \hat{a}_s^{\dagger 3} \hat{a}_s^3, \quad (1) \end{aligned}$$

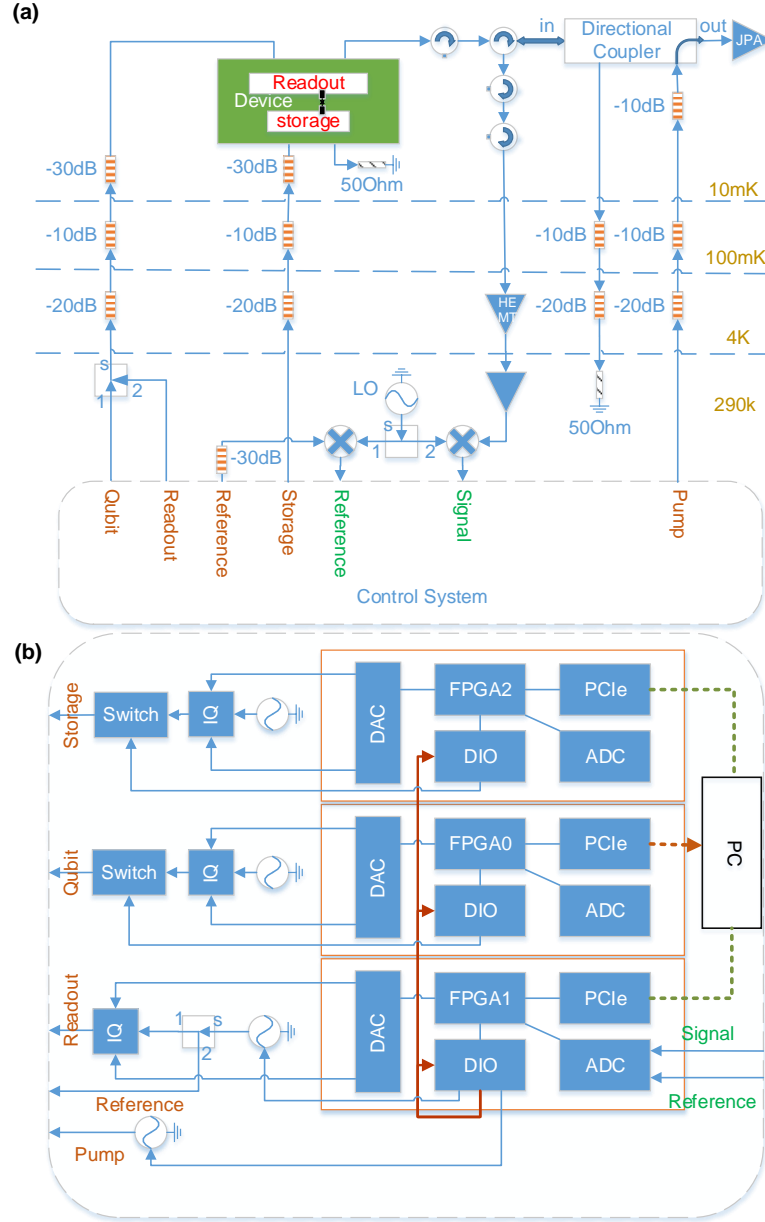


FIG. S1. **Experimental setup.** (a) Details of wiring and circuit components. The experimental device has a transmon qubit (the ancilla) dispersively coupled to both a readout cavity and a storage cavity (the oscillator). The cavities are made of high purity 5N5 aluminum and are chemically etched to improve coherence time. A JPA is located at 10 mK, after two circulators, allowing for a high-fidelity single-shot measurement of the ancilla. A high-electron-mobility-transistor (HEMT) amplifier at 4 K and an amplifier at room temperature are also used before the down-conversion of the signal to 50 MHz with a local oscillator (LO). Part of the readout signal does not go through the dilution refrigerator and is used as a reference to lock the phase of the returning readout signal from the device for a better measurement stability. (b) The FPGA control system. Three X6-1000M boards and a VPXI-ePC from Innovative Integration are used to control the qubit (FPGA0), the readout cavity (FPGA1), and the oscillator (FPGA2). Each board contains two DACs, two ADCs, and 64 independent DIO ports (as input or output). The control pulse envelopes modulated at 100 MHz are generated from DACs. Microwave switches are used for the qubit and the oscillator control signals for better protection against leakage and are controlled by the DIO port on the corresponding board. Both microwave generators for the readout and the JPA pump work in a pulsed mode controlled by the DIO ports as well. The down-converted returning readout signal from the device is fed into the ADCs on the same FPGA board (FPGA1) that also sends out the readout signal. The demodulation and calculation are performed inside FPGA1 and the results are discriminated into digitized signals. These final readout signals are not only sent to the host PC, but also distributed among all FPGAs through the DIO ports for inter-board communication. The feedback operations coordinated among all three boards depend on the same digitized readout result.

\bar{n}	Parity fidelity
0	98.8%
1	97.8%
2	97.2%
3	97.1%

TABLE III. Average parity measurement fidelity vs \bar{n} based on the protocol ($R_{\pi/2}^Y$, π/χ_{qs} , $R_{-\pi/2}^Y$). The single parity measurement is 99.92% QND (see Fig. S4 below).

where $\omega_{q,s,r}$ are the ancilla qubit, the oscillator, and the readout cavity frequency, respectively; $\hat{a}_{q,s,r}$ are the corresponding ladder operators; χ_{qs} , χ_{qr} , χ_{sr} are the cross-Kerrs; $K_{q,r,s}$ are the self-Kerr of corresponding quantum system; and K'_s is a higher-order correction to the self-Kerr K_s . All these parameters are either measured directly or derived from the measured ones, and are displayed in Table I. It is worth noting that although K'_s is not shown explicitly in Eq. 3 in the main text, it is important to take it into account when calculating the control pulses based on the gradient ascent pulse engineering (GRAPE) method [9, 10] and choosing the right waiting interval for the measurement of the uncorrected binomial code decay time. K_s and K'_s of the oscillator are estimated by measuring the phase of $|2\rangle$ and $|4\rangle$ relative to $|0\rangle$ after an evolution of the initial state $(|0\rangle + |2\rangle)/\sqrt{2}$ and $(|0\rangle + |4\rangle)/\sqrt{2}$, respectively, as shown in Fig. S2.

The coherence times and thermal populations of all modes are summarized in Table II. The ancilla qubit has an energy relaxation time $T_1 = 30.0 \mu\text{s}$ and $T_2 = 40.0 \mu\text{s}$ corresponding to a pure dephasing time $T_\phi = 120 \mu\text{s}$. The ancilla qubit has a steady-state excited state population of $n_{\text{th}}^q = 0.008$, presumably due to stray infrared photons or other background noise leaking into the system. Together with the measured $T_1 = 30.0 \mu\text{s}$, we can derive the effective time for the ancilla being excited by thermal environment as $1/\Gamma_\uparrow \approx 3750 \mu\text{s}$, which is much larger than the duration of our experiment. The oscillator has a single-photon lifetime $\tau_s = 143 \mu\text{s}$ ($\kappa_s/2\pi = 1.1 \text{ kHz}$) and a coherence time $T_2^s = 252 \mu\text{s}$ corresponding to a pure dephasing time $T_\phi^s = 2.1 \text{ ms}$. The dephasing time of the cavity is more than an order of magnitude larger than the photon energy relaxation time, justifying the argument that photon decay is the main decoherence channel for the logical qubit. Due to the strong interaction between the oscillator and the ancilla qubit, the pure dephasing time of the oscillator during idle when the ancilla qubit is in its ground state apparently is mainly limited by the ancilla qubit thermal noise as $1/\Gamma_\uparrow$. However, for operations assisted by the ancilla qubit, the excitation of the qubit could introduce significant dephasing. Since this effect is combined with other imperfections, we do not separately estimate the dephasing of the operations but just include it in our numerically and experimentally estimated operation fidelities. Thus, further suppressing the ancilla qubit thermal excitation and extending the ancilla qubit energy decay time are essential to eliminate the dephasing channel of the oscillator. Based on a similar ar-

gument, due to the strong-dispersive interaction between the ancilla qubit and the readout cavity, thermal population of the readout cavity can limit the ancilla qubit pure dephasing time $T_\phi < 1/n_{\text{th}}^r \kappa_r$ [11]. Based on the measured ancilla qubit dephasing time, we can obtain an upper limit on the thermal population of the readout cavity $n_{\text{th}}^r < 0.0004$. The thermal population of the oscillator $n_{\text{th}}^s \sim 0.006$ is derived based on parity measurements in its steady state (see below).

The dispersive interaction between the ancilla qubit and the readout cavity χ_{qr} , nearly matched with the decay rate κ_r of the readout cavity for an optimal signal-to-noise ratio, enables a high-fidelity (with the help of a JPA) and high quantum non-demolition (QND) single-shot readout of the ancilla qubit [12]. The readout pulse has been optimized to have a width of 320 ns at a few-photon (< 10) level. The readout fidelity is > 0.999 for $|g\rangle$ and 0.989 for $|e\rangle$ (Figs. S3a and S3b). The readout fidelity loss for $|e\rangle$ comes from the ancilla qubit decay during the measurement time. The readout fidelity of the ancilla qubit measured at $|g\rangle$ when initially prepared in $|g\rangle$ by post-selection is > 0.999 , while the fidelity for $|e\rangle$ state when initially prepared in $|e\rangle$ by post-selection is 0.974 (Figs. S3c and S3d). The readout fidelity loss for $|e\rangle$ is dominantly due to the ancilla qubit decay during the following waiting time (320 ns) and measurement time (320 ns), demonstrating the highly QND nature of the dispersive readout.

The dispersive interaction between the ancilla qubit and the oscillator χ_{qs} allows one to do a Ramsey-type parity measurement of the photon numbers in the oscillator [13], where two unconditional $\pi/2$ rotations ($R_{\pi/2}^Y$) of the ancilla qubit are separated by a pure delay of π/χ_{qs} . Since in our QEC experiment the ancilla qubit is always prepared in the ground state (a π pulse is applied if the ancilla qubit is measured in $|e\rangle$) and logical qubit has an even parity, we only focus on the parity measurement protocol ($R_{\pi/2}^Y$, π/χ_{qs} , $R_{-\pi/2}^Y$) in order to return the ancilla to $|g\rangle$ if the parity is even. The $\pi/2$ rotation pulses have a Gaussian envelope truncated to $4\sigma = 20 \text{ ns}$ with the so-called ‘‘derivative removal by adiabatic gate’’ (DRAG) technique [14].

Due to the finite bandwidth of the $\pi/2$ rotations, the parity readout fidelities depend on the average number of photons in the cavity, which is characterized following a similar technique in Ref. 15. An initialization of the system based on post-selections creates a vacuum state in the oscillator and ground state of the ancilla qubit. Then a cavity displacement $D(\alpha = \sqrt{\bar{n}})$ and three consecutive parity measurements are performed. Post-selections of the first two consecutive identical parity results would give a photon state parity with good confidence, and the third parity measurement is used for the final parity fidelity measurement. The averaged parity measurement fidelity results are listed in Table III. Note that for the protocol ($R_{\pi/2}^Y$, π/χ_{qs} , $R_{-\pi/2}^Y$), the fidelity for an odd parity state is slightly lower than an even parity state because the ancilla qubit ends up in the excited state which has the possibility of an extra decay during the following ancilla qubit readout. The most relevant number in our experiment is for

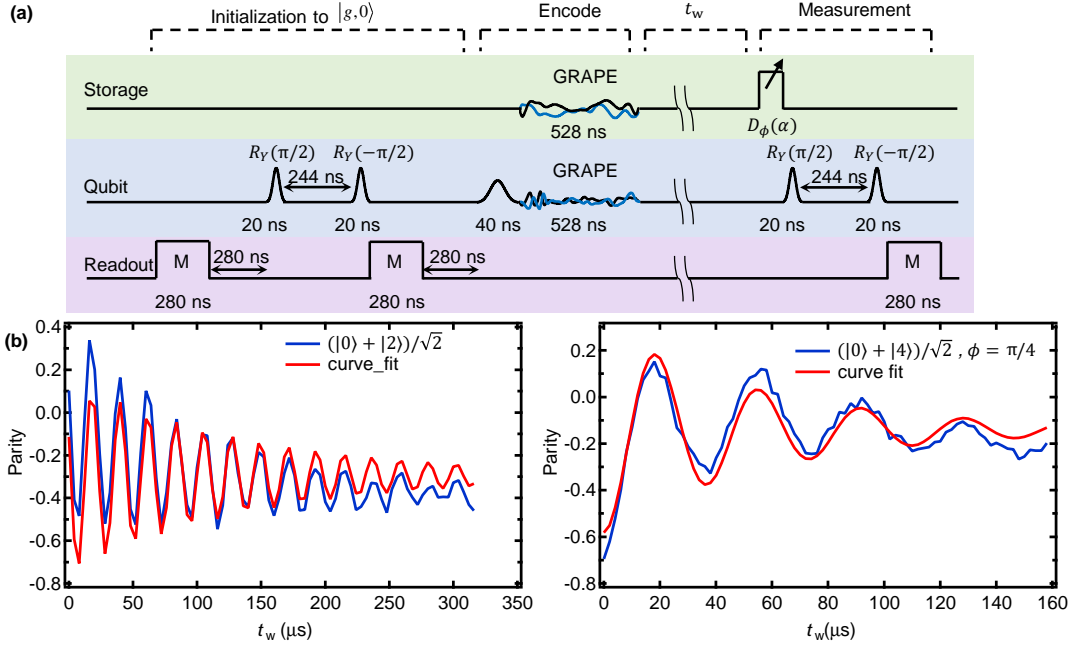


FIG. S2. **Measurements of Kerr coefficients for the oscillator.** (a) The measurement sequence. We encode the oscillator into $(|0\rangle + |2\rangle)/\sqrt{2}$ and $(|0\rangle + |4\rangle)/\sqrt{2}$ for measuring K_S and K'_S , respectively. t_w varies with a step of $4\ \mu\text{s}$ for $(|0\rangle + |2\rangle)/\sqrt{2}$ and $2\ \mu\text{s}$ for $(|0\rangle + |4\rangle)/\sqrt{2}$. Then a parity measurement is performed following a displacement operation on the oscillator with $\alpha = 0.7\sqrt{2}$ for $(|0\rangle + |2\rangle)/\sqrt{2}$ and $\alpha = 0.9\sqrt{2}$ for $(|0\rangle + |4\rangle)/\sqrt{2}$. The phase of the displacement operation ϕ varies for $(|0\rangle + |2\rangle)/\sqrt{2}$ or is fixed at $\pi/4$ for $(|0\rangle + |4\rangle)/\sqrt{2}$. (b) Measured parity oscillations. Fitting the curves using $y = y_0 + Ae^{-t/\tau}\cos(\omega t + \phi_0)$ gives the frequencies of the oscillation, from which we derive the Kerr coefficients by subtracting the known detuning: the self-Kerr $K_S/2\pi = 4.23\ \text{kHz}$ (in the term $-\frac{K_S}{2}\hat{a}_s^{\dagger 2}\hat{a}_s^2$) and the correction to the self-Kerr $K'_S/2\pi = 454\ \text{Hz}$ (in the term $-\frac{K'_S}{6}\hat{a}_s^{\dagger 3}\hat{a}_s^3$).

$\bar{n} = 2$, and the corresponding averaged parity readout fidelity is 0.972 (98.3% for an even parity and 96.0% for an odd parity).

The QND nature of the error syndrome measurement (that does not introduce extra photon jump errors) is essential for QEC. To quantify the QND property of the parity measurement on the oscillator, the parity decay of a coherent state is monitored by performing repeated parity measurements ($R_{\pi/2}^Y$, π/χ_{qs} , $R_{-\pi/2}^Y$) with different intervals, 1 – 30 μs . This experiment is carried out with real-time feedback which always flips the ancilla qubit back to the ground state after each parity measurement in order to eliminate the ancilla qubit decay during the interval between parity measurements. The averaged parity decay curves vs time with an initial displacement $\alpha = \sqrt{2}$ are shown in Fig. S4 and are fitted with $\langle P \rangle = \frac{1+P_0}{2}(2P_e - 1) + \frac{1-P_0}{2}(1 - 2P_o)$, where $P_0 = e^{-2|\alpha|^2 e^{-t/\tau_{\text{tot}}}/(1+2n_{\text{th}}^s)}/(1+2n_{\text{th}}^s)$ is the expected parity evolution with a steady-state thermal population n_{th}^s in the cavity, τ_{tot} is the parity decay time under monitoring, and P_e (P_o) is the parity measurement fidelity for an even (odd) state. The fit gives $n_{\text{th}}^s \sim 0.006$. The extracted τ_{tot} vs repetition interval is shown in the inset of Fig. S4. The total decay time is well modelled by a parallel combination of the natural decay (τ_s) and a constant demolition probability $p_d = 0.08\%$ per measurement, indicating that a single parity measurement is

99.92% QND.

EXPERIMENTAL SEQUENCES

In the following, we show the details of our experimental sequences. Since both the ancilla qubit and the oscillator have non-zero but small thermal excitations, we always initialize our system to $|g,0\rangle$ (the notation denotes $|qubit, oscillator\rangle$) by post-selection on the ancilla qubit's ground state and a subsequent oscillator parity measurement. This post-selection only removes about 1.4% of the total data, so we do not use an adaptive control to perform the initialization, although in principle we could.

The ancilla qubit plays two main roles: 1) serve as an ancilla for the error syndrome detection of the logical qubit; 2) provide the necessary non-linearity for implementing all the operations related to the oscillator including encoding, decoding, error correcting, as well as the universal single logical qubit operations. Through a sequence of control pulses on the system, all these operations on the logical qubit are realized based on the dispersive interaction between the ancilla and the oscillator. The control pulses are synchronized and generated by FPGAs with home-made logic. The pulse shapes are numerically optimized with GRAPE [9, 10] based on carefully calibrated experimental parameters. All GRAPE pulses have

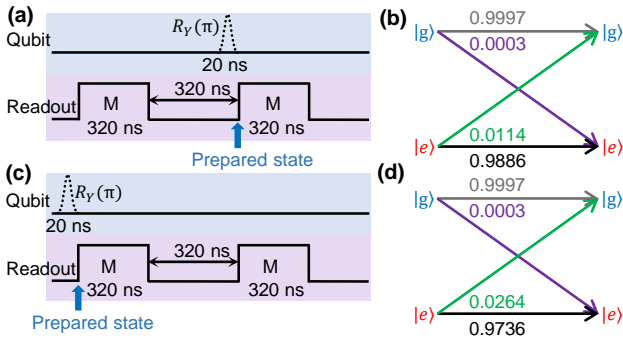


FIG. S3. **Readout property.** (a) Sequences for readout fidelity determination. The ancilla qubit is first measured and the ground state $|g\rangle$ is post-selected, then no π pulse or a π pulse is performed to prepare $|g\rangle$ or $|e\rangle$ followed immediately by a second readout measurement. (b) Readout fidelity corresponding to the sequences in (a). The readout fidelity is > 0.999 for $|g\rangle$ and 0.989 for $|e\rangle$. The readout fidelity loss for $|e\rangle$ comes from the ancilla qubit decay during the measurement time. (c) Sequences to test QND. No π pulse or a π pulse is performed to prepare a state with dominant $|g\rangle$ or $|e\rangle$ followed by the first readout. After a waiting time of 320 ns, a second readout is performed. (d) Readout fidelity corresponding to sequences in (c). The readout fidelity for $|g\rangle$ when initially prepared in $|g\rangle$ by post-selection is > 0.999 , while the fidelity for $|e\rangle$ when initially prepared in $|e\rangle$ by post-selection is 0.974 . The readout fidelity loss for $|e\rangle$ is dominantly due to the ancilla qubit decay during the waiting time and measurement time, demonstrating the highly QND nature of the readout.

a duration of 528 ns in our experiment.

Figure S5 shows the measurement sequence for the process fidelity decay of the uncorrected Fock $\{|0\rangle, |1\rangle\}$ encoding. The sequence for the case of uncorrected binomial encoding (Fig. S6) is similar except that the waiting times are chosen such that the Kerr rotations of $|4\rangle$ are integer multiples of 2π to minimize the deformation of one of the code space bases $(|0\rangle + |4\rangle)/\sqrt{2}$. This is because in our experiment we have chosen a rotating frame of ω_s so that both $|4\rangle$ and $|2\rangle$ rotate relative to $|0\rangle$ due to the Kerr effects. In principle, we can choose another frame to match the rotation of $|4\rangle$ relative to $|0\rangle$ by rotating at $\omega_{4s}/4$, where ω_{4s} is the frequency difference between $|0\rangle$ and $|4\rangle$ of the cavity. Note that this is true even if the higher-order corrections to Kerr are taken into account, which is one of the nice features of the lowest-order binomial code [16]. The extra phase associated with $|2\rangle$ is deterministic and is corrected in our final analysis after decoding.

Figures S7 and S8 show our repetitive QEC sequence and the details of the QEC process, respectively. The latency of our adaptive control is defined as the time interval between receiving the last point of the readout signal and sending out the first point of control signal including the speed of light travel time through the whole experimental circuitry and is only 336 ns, about 1% of the ancilla qubit lifetime.

T GATE FIDELITY USING REPEATED MEASUREMENTS

The T gate does not belong to the Clifford group, so it can not be characterized by randomized benchmarking. We instead perform repeated gates to extract the gate fidelity of 0.987 , as shown in Fig. S9. This fidelity has been converted to be consistent with the fidelity definition in the randomized benchmarking method. We note that if the noise channel is a depolarization channel and the probability of having a full depolarization is p , then in the randomized benchmarking experiment the fidelity $F_{\text{RB}} = 1 - p/2$. However, the χ matrix decay curve with respect to the number of repeated gates gives the normalized process fidelity (Eq. 3 defined below) $F = 1 - p$.

THEORETICAL ANALYSIS AND ERROR MODEL OF THE QEC PERFORMANCE

In the QEC experiment, the ancilla plays multiple critical roles, including in the encoding, decoding, error detection, error correcting recovery operation, and the universal single logical qubit operations. The decoherence of the ancilla introduces imperfections for the above processes and thus eventually limits the ultimate performance of our current experiment. As just mentioned, on one hand, the ancilla facilitates the error detection, correction, and gate operations. Therefore, errors in these processes due to the ancilla decoherence prevent too frequent repetitive QEC process. On the other hand, with a larger interval between QECs, there is a higher probability of having undetectable higher-order photon loss and gain errors and a larger dephasing effect induced by photon losses (due to the non-commutativity of the annihilation operation \hat{a}_s and the self-Kerr term $\frac{K_s}{2} \hat{a}_s^\dagger \hat{a}_s^2$). These two types of error, caused by the intrinsic cavity photon loss and the operations facilitated by the ancilla, compete with each other and ultimately lead to an optimization of the QEC performance.

In order to understand the experimental results of the QEC performance, in this section we first investigate the two types of errors in detail, and then establish an approximate analytical model that applies to two experimental protocols, Protocol I and Protocol II for one and two bottom-layer detections and corrections respectively. The model can explain both experiments well and thus also indicates the possible routes to further improve the performance of the binomial code QEC in the future. The scheme and results of Protocol II have been shown in the main text already. The experimental procedure of Protocol I is depicted in Fig. S10, in which the recovery gates are performed immediately in both no-error and one-error cases after each detection.

Both analytical models that are based on a simple error propagation treatment and numerical simulations that are based on QuTiP in Python [17, 18] have been adopted to analyze each sub-process of the whole QEC protocol. Although the analytical model provides more physical insights, the numerical approach can be more rigorous. To compare with the experiments, the decoherence of the ancilla and the oscillator

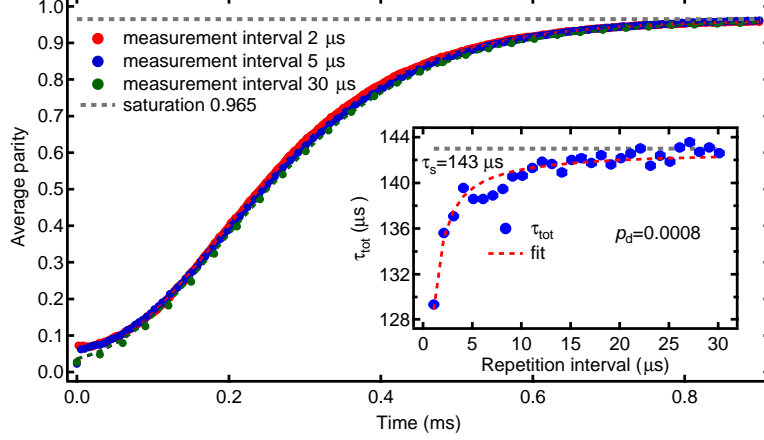


FIG. S4. **QND property of the parity measurement.** To quantify the QND property of the parity measurement on the oscillator, the parity decay of a coherent state is monitored by performing repeated parity measurements ($R_{\pi/2}^Y, \pi/\chi_{qs}, R_{-\pi/2}^Y$) with different intervals, 1 – 30 μs . This experiment is carried out with feedback which always flips the ancilla qubit back to the ground state after each parity measurement in order to eliminate the ancilla qubit decay during the interval between parity measurements. The main figure shows the averaged parity decay curves vs time with three typical repetition intervals: 2 μs , 5 μs , and 30 μs with an initial displacement $\alpha = \sqrt{2}$. In the large time limit, the cavity reaches a thermal steady state with a thermal population n_{th}^s and each curve saturates at $\langle P \rangle = 0.965$ (due to finite n_{th}^s and parity measurement fidelities). Dotted lines are fits with $\langle P \rangle = \frac{1+P_0}{2}(2P_e - 1) + \frac{1-P_0}{2}(1 - 2P_o)$, where $P_0 = e^{-2|\alpha|^2 e^{-1/\tau_{tot}}/(1+2n_{th}^s)}/(1+2n_{th}^s)$ is the expected parity evolution with a steady-state thermal population n_{th}^s in the cavity, τ_{tot} is the parity decay time under monitoring, and P_e (P_o) is the parity measurement fidelity for an even (odd) state. Note that both P_e and P_o slightly depend on the average photon number in the cavity and here we choose $P_e = 0.987$ and $P_o = 0.969$ for an averaged $\bar{n} = 1$. The fit also gives $n_{th}^s \sim 0.006$. The humps when time is small for intervals 2 μs and 5 μs are mainly due to the ancilla qubit decay during the feedback latency time (336 ns). The insert shows the extracted τ_{tot} vs the repetition interval τ_{rep} . The error bar is derived from bootstrapping of each curve (80,000 averages) in the main figure. Under parity monitoring, τ_{tot} and the natural decay rate τ_s obey the relationship $1/\tau_{tot} = 1/\tau_s + p_d/\tau_{rep}$, where the p_d is the probability of inducing an extra parity change by the parity measurement [13]. A fit gives $1/\tau_s = 143 \mu\text{s}$ and $p_d = 0.08\%$, indicating that a single parity measurement is 99.92% QND.

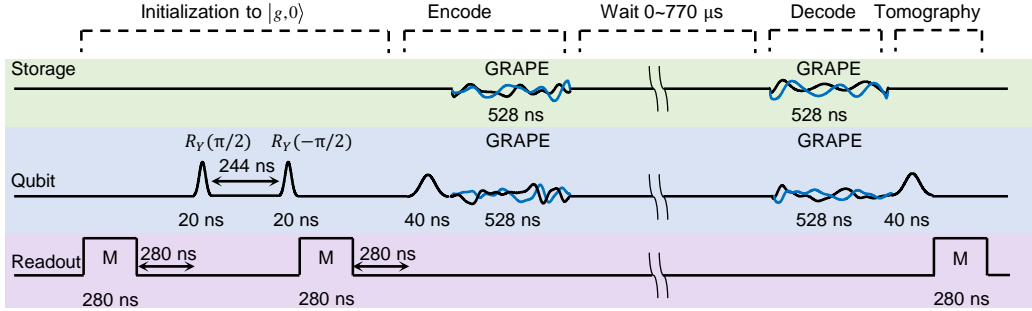


FIG. S5. **Experimental sequence to measure the uncorrected Fock $\{|0\rangle, |1\rangle\}$ encoding lifetime.** The whole experiment can be divided into five parts: initialization of the system to $|g, 0\rangle$, encoding, various waiting time, decoding, and final state tomography of the ancilla. The encoding and decoding are realized by GRAPE pulses. The final state tomography of the ancilla is realized by pre-rotations of the ancilla qubit followed by a σ_z projection measurement.

are included in the numerical simulations through the Lindblad master equations. In the interaction picture, the simplified Hamiltonian used in the simulation is

$$H_{\text{int}} = -\chi_{qs} a_s^\dagger a_s |e\rangle \langle e| - \frac{K_s}{2} a_s^{\dagger 2} a_s^2 - \frac{K'_s}{6} a_s^{\dagger 3} a_s^3. \quad (2)$$

Here we treat the ancilla as a two-level system and ignore the readout cavity. The parameters in the numerical simulations

are taken from the calibrated experimental parameters, which have been listed in Tables I and II.

Since the minimum process fidelity (F_χ) is 0.25, in the following we denote the fidelity as the normalized process fidelity with a full scale between 0 and 1:

$$F = (F_\chi - 0.25)/0.75. \quad (3)$$

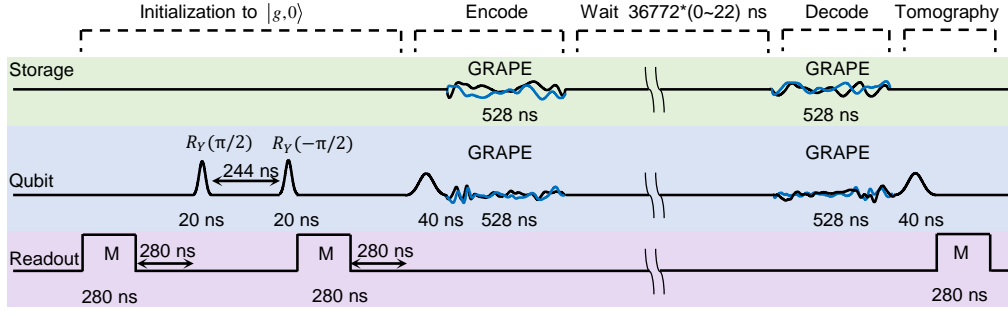


FIG. S6. **Experimental sequence to measure the uncorrected binomial encoding lifetime.** The GRAPE pulses for encoding and decoding are the same as those in the QEC experiment. The waiting intervals $t_w = N \times 36,772$ ns ($N = 0 - 22$) between encoding and decoding are chosen such that the Kerr rotations of $|4\rangle$ are integers of 2π . However, the phase of $|2\rangle$ is $N\phi_0$ that is deterministic due to the self-Kerr of the oscillator. After decoding, this phase is transferred to $|e\rangle$ state and is corrected in the data analysis.

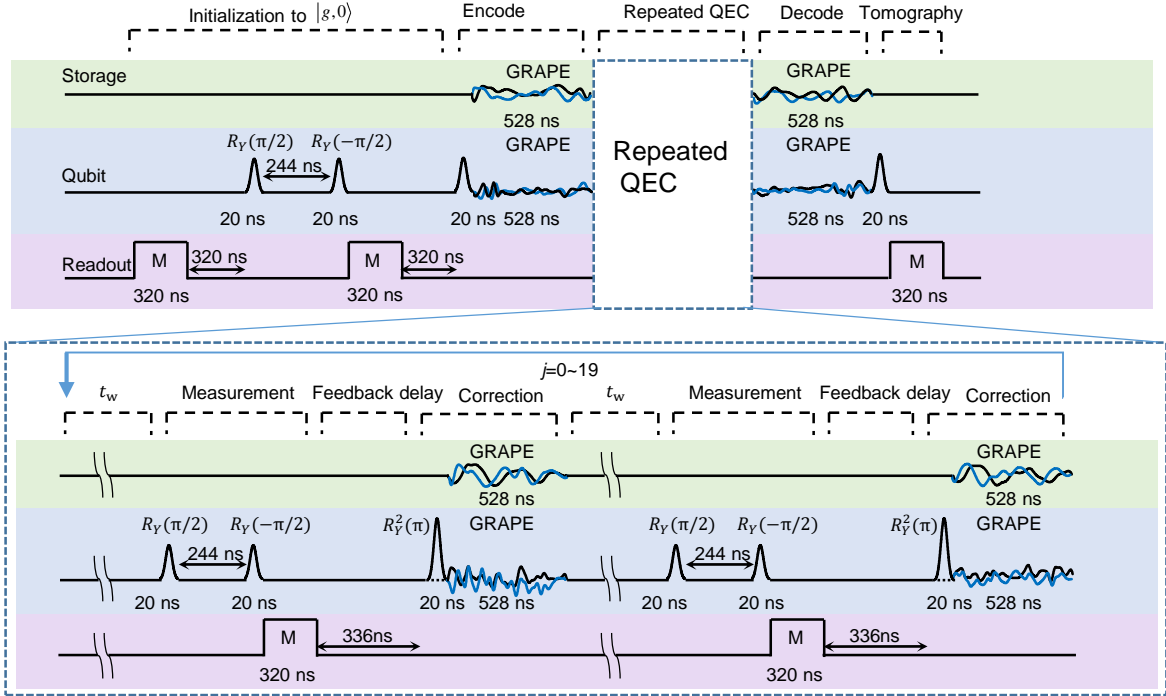


FIG. S7. **Experimental sequence for the repetitive QEC.** The essential part is the two-layer QEC procedure. The top layer recovers the quantum information in the code space and is repeated 0-19 times. Two bottom-layer processes are used to conserve parity in the deformed code space. Each bottom-layer process consists of a waiting time $t_w = 17.895$ μ s, error detection, feedback delay, and correction. If no error is detected, the π rotation is replaced by a pure waiting time. Appropriate recovery GRAPE pulses are performed depending on the error detection results as shown in the protocol of Fig. 2a in the main text.

Intrinsic Errors from Oscillator Photon Loss

The binomial code implemented in this experiment can protect quantum information against a single photon loss error \hat{a}_s . In principle, frequent error correction would suppress the higher order errors, i.e. $(\tau_w/\tau_s)^n$ vanishes when $\tau_w/\tau_s \ll 1$, where τ_w is the time interval between QEC steps, τ_s is the previously defined single-photon lifetime, and $n > 1$. However, due to the imperfections in both error detection and correction (discussed below), τ_w should not be too small. In this case, there are errors intrinsic to this encoding: the errors that

are not contained in the error set $\{\hat{f}, \hat{a}_s\}$ would cause a failure of the performance. The intrinsic errors include: (1) multiple photon losses for finite τ_w/τ_s , which could not be detected and corrected. (2) the photon gain error due to thermal noise injected into the oscillator. (3) the dephasing due to the combination of photon loss jump and the self-Kerr effect. Since the detected single photon loss may happen in any time during τ_w , the photon-number dependent Kerr phase accumulation should depend on the jump time, which induces a phase correlation between the oscillator and the leaked photon and eventually gives rise to dephasing. (4) the non-unitary no-

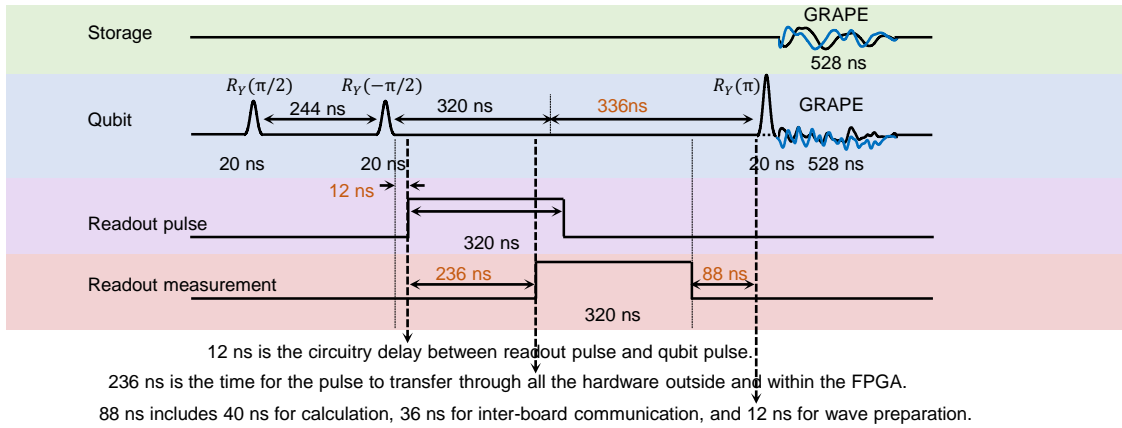


FIG. S8. **Details of the QEC process.** Different FPGA boards are synchronized to control the readout, the ancillary qubit, and the oscillator. The FPGAs to control the ancilla qubit and the oscillator are the same with no relative delay, but both have a relative delay with the one to control the readout. The feedback delay contains three parts: 1) the delay between the readout pulse and ancilla qubit pulse due to the control circuitry difference; 2) the time taken by the signal travelling through the experimental circuitry outside and within the FPGA; 3) the time for calculation, inter-board-communication, and response to the adaptive instruction. The whole process takes 336 ns in our system.

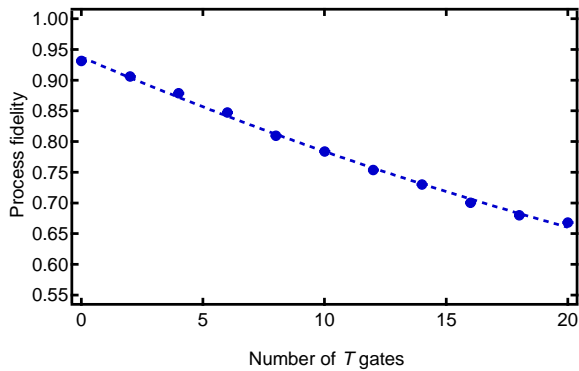


FIG. S9. **T gate process fidelity by repeated gate measurements.**

The T gate is repeated 0, 2, 4, ..., 20 times and the corresponding process fidelities are measured. A fit with $F_{\chi}(t) = 0.25 + Ae^{-t/\tau}$ gives $e^{-1/\tau} = 0.974$, implying a gate fidelity of 0.987 when converted to be consistent with the fidelity definition in the randomized benchmarking method. The intercept at $N = 0$ is the “round trip” process fidelity of the encoding and decoding processes only, same as Fig. 3a in the main text.

jump evolution $e^{-(\kappa/2)\hat{a}^{\dagger}\hat{a}t}$. The unitary recovery operations correct the non-unitary no-jump evolution only to first order in κt_w [16] as discussed in the main text.

To quantify the contribution of these errors, we numerically simulate the process including only the oscillator decay and Kerr terms without the ancilla qubit decoherence. We further construct ideal unitary encoding, decoding, and error correction gates, and implement ideal parity projection measurement. Figure S11 shows the process fidelities and the error detection probabilities as a function of the total interval T_w per round of top-layer QEC for the two different protocols. Note that for Protocol I $T_w \approx \tau_w$ and for Protocol II $T_w \approx 2\tau_w$

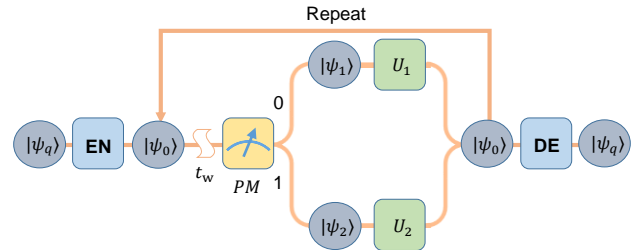


FIG. S10. **Procedure for QEC Protocol I.** The same encoding and decoding as in Fig. 2a in the main text are used here. However, the difference is that the detection and correction are performed in each QEC step. Process tomography is used to benchmark this QEC performance.

which is roughly twice as large as t_w for the bottom-layer QEC process in the main text.

The intrinsic errors for Protocol I are summarized by the parameters F_{i0} and F_{i1} , corresponding to the process fidelity for detecting no error (no photon loss) or one error (single photon loss) respectively. In addition, we also define p_0 as the probability of detecting no error. The case for Protocol II is more complicated because of two bottom-layer QECs. As shown in Fig. 2a in the main text, there are four different branches corresponding to four different process fidelities F_{i00} , F_{i01} , F_{i10} , and F_{i11} . The second subscript of F represents a detection of no error (0) and one error (1) in the first syndrome measurement, respectively, while the third subscript represents the result of the second syndrome detection. The probability of detecting no error for the first syndrome detection is p_0 , while p_{00} and p_{10} are the probability of detecting no error for the second syndrome detection provided no error or an error is detected in the first syndrome detection respectively. These fidelities and probabilities are all different for different branches because of the state differences. Note

that the error rates for $|0_L\rangle$ and $|1_L\rangle$ are slightly different and the probabilities plotted in Figs. S11a and S11b are calculated for the representative superposition state $(|0_L\rangle + |1_L\rangle)/\sqrt{2}$. When calculating the process fidelities, the backaction associated with the no-parity-jump evolution has been included.

For the no-error case, the dominant intrinsic error is due to the undetectable two photon losses. While for the one-error case, the main intrinsic error source is the Kerr dephasing coming from the fact that $[\hat{a}_s, \frac{K_s}{2}\hat{a}_s^\dagger\hat{a}_s^2] \neq 0$ and there is no way of knowing the exact time when a photon loss occurs. After one photon loss happens, the resulting photon state further suffers an amplitude damping because of the imbalance of the photon number between the error states $|3\rangle$ and $|1\rangle$. The errors due to three photon losses and one photon gain, which cause a leakage out of the logical space, are much smaller.

As shown in Fig. S11 and as expected, for both protocols the probability of no photon loss increases with decreasing T_w , and the intrinsic errors converge to zero in the limit $T_w \rightarrow 0$. However, a smaller QEC interval T_w means more frequent operations of error detection and correction, which cause extra errors mainly due to the ancilla decoherence as will be discussed below.

Parity Measurement Infidelity

Projective parity measurement with a protocol $(\pi/2, \pi/\chi_{qs}, -\pi/2)$ is constantly implemented to detect single photon loss errors in the QEC process. Therefore, a highly faithful parity measurement is critical for the QEC performance. However, during the parity measurement, ancilla qubit decoherence including both pure dephasing (T_ϕ) and energy relaxation (T_1) could cause the photon loss error detection to fail. The pure dephasing would give an incorrect indication of error detection, and then the quantum information would be completely destroyed by the following correction operation. If the ancilla qubit decays to the ground state during the parity measurement, with 50% probability the parity measurement would give a wrong indication and the quantum information would be completely destroyed as well. With the other 50% probability, the parity measurement would still give a correct indication. However, the part of the photon state entangled with the ancilla qubit's excited state would rotate by an unknown angle depending on the time when the ancilla qubit decays. This would cause both a leakage and a dephasing of the logical state, and the quantum information would also be strongly degenerated by the following operations, so this case can be treated as a complete destruction as well.

To simulate the projective measurement with a finite width (320 ns), we simply treat the projection in the simulation occurs at the middle point of the measurement pulse. Thus, we denote the time before and after the projection as $T_{BM} = 160$ ns and $T_{AM} = 496$ ns respectively, where the feedback latency time of 336 ns is included in T_{AM} . Since the parity measurement time $\sim \pi/\chi_{qs}$ is much shorter than both T_1 and

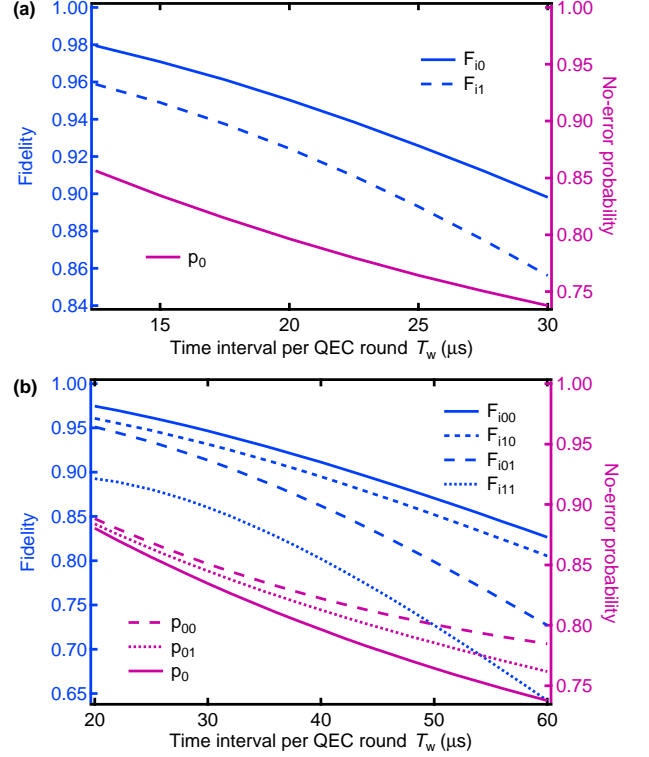


FIG. S11. **Intrinsic errors for the binomial code.** In the numerical simulations, only the cavity decay and Kerr effects have been included, neglecting ancilla qubit decoherence, detection error, and correction error. (a) Protocol I. F_{i0} and F_{i1} are the process fidelity (blue) for detecting no error and one error respectively. p_0 is the probability (purple) of detecting no error. (b) Protocol II. F_{i00} , F_{i10} , F_{i01} , and F_{i11} are the process fidelities for the following cases respectively: no error for both detections, no error for the first detection and one error for the second one, one error for the first detection and no error for the second one, one error for both detections. p_0 is the probability of detecting no error for the first syndrome detection, p_{00} is the probability of detecting no error for the second syndrome detection provided no error is detected in the first syndrome detection, p_{10} is the probability of detecting no error for the second syndrome detection provided an error is detected in the first syndrome detection. These fidelities and probabilities for different trajectories are different. Note that the error rates for $|0_L\rangle$ and $|1_L\rangle$ are slightly different and here the probabilities in both (a) and (b) are calculated from the representative superposition state $(|0_L\rangle + |1_L\rangle)/\sqrt{2}$. When calculating the process fidelities, the backaction associated with the no-parity-jump evolution has been included.

T_ϕ , the parity measurement process fidelity F_0 and F_1 , for an initial even and odd parity state respectively, can be approximated by linear functions of the ancilla qubit decoherence rates:

$$F_0 = C_0 - \pi/2\chi_{qs}T_1 - \pi/2\chi_{qs}T_\phi, \quad (4)$$

and

$$F_1 = C_1 - \pi/2\chi_{qs}T_1 - (T_{AM} + T_{BM})/T_1 - \pi/2\chi_{qs}T_\phi, \quad (5)$$

where C_0 and C_1 correspond to the parity fidelity when the ancilla qubit has no decoherence. Here F_1 has included the ancilla qubit energy relaxation during and after the projection measurement of the ancilla qubit (the second term in Eq. 5, since the ancilla qubit ends up in the excited state). Based on the measured parity readout fidelity $F_0 = 0.983$ and $F_1 = 0.960$ with $T_1 = 30 \mu\text{s}$ and $T_\phi = 120 \mu\text{s}$, we can derive $C_0 = 0.988$ and $C_1 = 0.987$. The deviation of C_0 and C_1 from unity could come from the non-ideal non-selective $\pi/2$ pulses in the parity measurement due to non-perfect amplitude calibration, finite bandwidth of the pulses, or possible calibration fluctuations.

Recovery Gate Infidelity

Numerically optimized pulses using the GRAPE method are implemented in the encoding, decoding, and correction processes. However, only the correction pulse infidelity contributes to the QEC process fidelity decay. Because the GRAPE pulses correspond to complex trajectories of both the ancilla qubit and the oscillator evolution, it is not intuitive to estimate the effects from the ancilla qubit decoherence during these pulses. Instead, we numerically simulate the recovery GRAPE pulse process fidelity in the presence of ancilla qubit decoherence, and extract the fidelity change as a function of the ancilla qubit decoherence T_1 and T_ϕ . Since the GRAPE pulse duration is much shorter than both T_1 and T_ϕ , the dependence of the process fidelity on the ancilla qubit decoherence is expected to be linear as the case for the parity fidelity above:

$$F_{U_3} = 0.978 - 0.233/T_1 - 0.181/T_\phi, \quad (6)$$

and

$$F_{U_2} = F_{U_4} = 0.976 - 0.173/T_1 - 0.188/T_\phi, \quad (7)$$

where U_2 , U_3 , and U_4 are the recovery gates defined in Fig. 2a in the main text, and here both T_1 and T_ϕ are in units of μs . It is difficult to experimentally calibrate the fidelities of the recovery GRAPE pulses directly, because both preparation of the initial state and measurement of the final state also require GRAPE pulses. Since the optimization procedure, pulse duration, and hardware are all the same, we assume the fidelities of all gates implemented by GRAPE pulses are the same. The two constants (the first terms) are determined by the extracted gate fidelity $F_U = 0.970$ when $T_1 = 30 \mu\text{s}$ and $T_\phi = 120 \mu\text{s}$ in our measured QEC process fidelity decay time, as shown in Fig. 3b in the main text.

Analytical Model and Error Propagation

With the assistance of the numerical simulations, errors from each individual component in the whole process can be estimated. Table IV shows the summarized error budget for the process fidelity loss in Protocol II with $t_w = 17.9 \mu\text{s}$

TABLE IV. Error budget for the process fidelity loss in Protocol II with $t_w = 17.9 \mu\text{s}$ ($T_w \approx 36 \mu\text{s}$) as in the main text. Case 00, case 01, case 10, and case 11 are for the following four cases respectively: no error for both detections, no error for the first detection and one error for the second, one error for the first detection and no error for the second, one error for both detections. Note that the total fidelity is the product of all individual fidelities. The total weighted average total error gives a decay time of the process fidelity of $198 \mu\text{s}$, in a good agreement with the experiment.

error source	case 00	case 01	case 10	case 11
for process fidelity loss				
intrinsic	7.0%	8.6%	11.0%	16.6%
detection	3.4%	5.6%	5.6%	7.7%
recovery	3.1%	3.2%	6.2%	6.2%
ancilla thermal excitation	0.7%	0.7%	0.7%	0.7%
total error	13.6%	17.0%	21.8%	28.3%
weighted average total error	16.2%			

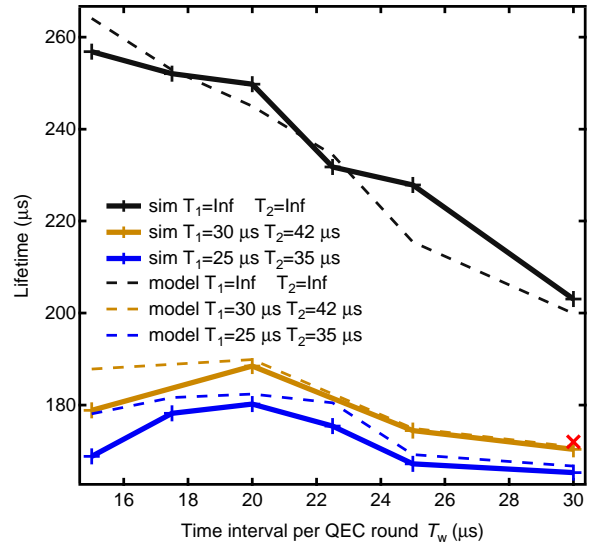


FIG. S12. **Predictions by numerical and analytical approaches for QEC Protocol I.** Curves with different colors present the QEC process fidelity decay time as a function of the QEC interval T_w with different ancilla qubit coherence times. The curves are not smooth because different optimized recovery pulses with different fidelities are used for different QEC intervals. Nevertheless, the good agreement between numerical simulations and the model using Eqs. 8 and 9 confirms the reliability of the model. The red cross indicates our experimental result ($T_1 = 30 \mu\text{s}$ and $T_2 = 40 \mu\text{s}$), also in good agreement with the simulation.

($T_w \approx 36 \mu\text{s}$) as in the main text. These numbers are obtained from numerical simulations with the capability of choosing individual error sources separately. In the simulations, the imperfections in the experiment associated with the parity measurement and the recovery gates as mentioned above have been taken into account. The total weighted average total error gives a decay time of the process fidelity of $198 \mu\text{s}$, in good agreement with the experiment.

Since the numerical simulation is time-consuming and does not provide physical intuition, we establish an analytical model for the error propagation during the QEC process based on a simplified probability calculation. With all the errors for individual operations in hand, we can study the fidelity of the whole QEC process. Here, we study Protocol I with one bottom-layer detection and correction first.

As errors occur in a probabilistic way, the fidelity after one QEC step in Protocol I could be described by the following equation:

$$F^{(I)}(T_w) = \underbrace{[p_0 F_{i0}(T_w) F_0 F_{U_1}]_{0 \text{ photon loss}} + \underbrace{[(1-p_0) F_{i1}(T_w) F_1 F_{U_2}]_{1 \text{ photon loss}}}_{\times [1 - n_{\text{th}}^q (1 - e^{-T_w/T_1})]}_{\text{no ancilla thermal flip}} \quad (8)$$

The expression consists of two branches: the process conditioned on no photon loss and the process conditioned on a single photon loss. Here, F_{U_1} and F_{U_2} are the fidelity of the recovery gate U_1 and U_2 shown in Fig. S10, respectively, and the last factor takes into account the small probability of the excitation of the ancilla to $|e\rangle$ during the waiting time T_w . $F^{(I)}(T_w)$ is then used to estimate the decay time τ of the QEC process according to an exponential decay:

$$\tau \approx -\frac{T_w}{\ln(F(T_w))}. \quad (9)$$

Figure S12 shows the QEC process fidelity decay time with different ancilla qubit coherence times as a function of the QEC interval t_w . The good agreement between numerical simulations and the analytical model using Eqs. 8 and 9 confirms the reliability of our model. Our experimental result with $T_1 = 30 \mu\text{s}$ and $T_2 = 40 \mu\text{s}$ ($T_\phi = 120 \mu\text{s}$) is also in a good agreement with the simulation.

The error propagation model in QEC Protocol II can be treated in a similar way but with more probabilistic branches:

$$F^{(II)}(T_w) = \underbrace{[p_0 p_{00} \cdot F_{i00}(T_w) \cdot F_0 \cdot F_0 \cdot F_{U_3}]_{0 \text{ photon loss for both detections}}} + \underbrace{[p_0(1-p_{00}) \cdot F_{i01}(T_w) \cdot F_0 \cdot F_1 \cdot F_\pi \cdot F_{U_4}]_{0 \text{ photon loss for the first; 1 photon loss for the second detection}}} + \underbrace{[(1-p_0)p_{10} \cdot F_{i10}(T_w) \cdot F_1 \cdot F_\pi \cdot F_{U_2} \cdot F_0 \cdot F_{U_3}]_{1 \text{ photon loss for the first; 0 photon loss for the second detection}}} + \underbrace{[(1-p_0)(1-p_{10}) \cdot F_{i11}(T_w) \cdot F_1 \cdot F_\pi \cdot F_{U_2} \cdot F_1 \cdot F_\pi \cdot F_{U_4}]_{1 \text{ photon loss for both detections}}} \cdot \underbrace{[1 - n_{\text{th}}^q (1 - e^{-T_w/T_1})]}_{\text{no ancilla thermal flip}}, \quad (10)$$

with all the parameters defined earlier. Compared to the no-error case (F_{U_3}), the one-error cases (F_{U_2} and F_{U_4}) have an additional error source from the preceding π pulse. The error associated with this π pulse can completely destroy the encoded quantum information through the following recovery

gates. Since the π pulse is so short, its dependence on the ancilla qubit decoherence can be neglected. In the experiment, $F_\pi = 0.984$ with the infidelity mainly coming from the finite gate bandwidth and possible fluctuation of pulse calibration.

In order to optimize the QEC interval T_w (or t_w), in Fig. 3b in the main text we have plotted the QEC process fidelity decay time τ by using Eqs. 9 and 10 as a function of the interval per QEC round (T_w) while keeping all other parameters except for the recovery gate fidelity fixed. As expected, there is an optimized region of T_w for the longest logical qubit lifetime τ . In the experiment, a critical parameter is the fidelity of the GRAPE pulse F_U , which is difficult to calibrate separately as mentioned earlier. Therefore, we vary F_U from 0.95 to 1 with a step of 0.005 when plotting Fig. 3b in the main text. The measured lifetime $\tau = 200 \mu\text{s}$ implies $F_U = 0.970$, which is exactly the one to give the calibration for Eqs. 6 and 7. This recovery GRAPE pulse fidelity is mainly limited by the ancilla qubit and oscillator decoherence. The interval used in the experiment as expected coincides with the optimal one from the model.

Towards Break-Even Point

Although the lifetime of the logical qubit achieved in our experiment is close to that of the Fock $\{|0\rangle, |1\rangle\}$ encoding, there are still a few ways to achieve the break-even point which could be investigated experimentally in the future.

Improve the ancilla properties

As explained by Fig. 3c in the main text, improving the ancilla coherence properties is the most direct way to extend the QEC lifetime, because error detection and all recovery operations utilize the ancilla qubit. If the ancilla coherence times can be improved, our system can work with more frequent error detection and correction, thus reducing τ_w and suppressing further the intrinsic errors. Our model predicts that the break-even point could be achieved if T_1 can be nearly doubled even with the same T_ϕ .

Better parameter calibration and GRAPE pulses

The model described above has carefully analyzed the infidelities of the parity measurement and the recovery processes. Except for the contribution from the finite T_1 and T_ϕ of the ancilla, there are also parameter fluctuations that lead to the fidelities $C_{0,1} \sim 0.987$ for the parity measurement and 0.976 for the recovery gates. To minimize the parameter fluctuations, the parameters of the experimental system should be carefully calibrated and also be stabilized during the experiment. Then, the detection and corrections based on these parameters could allow us to control the system more precisely.

Increasing the number of bottom-layer QEC steps

Since the recovery gate introduces extra errors in the QEC process, it would be a better strategy to have the state after the deterministic evolution untouched as much as possible when no error is detected, i.e. to have more bottom-layer QEC steps, as shown in Fig. S13. We extend the model of Eqs. 8 and 10 to this case while reasonably assuming the same fidelities for error detection and recovery gates. The result is shown in Fig. S14. Note that the backaction associated with the no-parity-jump evolution has been included in the model. We estimate that if the number of bottom-layer QEC steps, which construct a single top-layer QEC process, were increased to four, the break-even point could be achieved with our current experimental system. However, this new strategy demands more adaptive gate calibrations, so it is not implemented in our current experiment but could be investigated experimentally in the future.

* These two authors contributed equally to this work.

† clzou321@ustc.edu.cn

‡ luyansun@tsinghua.edu.cn

- [1] M. Reagor, H. Paik, G. Catelani, L. Sun, C. Axline, E. Holland, I. M. Pop, N. A. Masluk, T. Brecht, L. Frunzio, M. H. Devoret, L. I. Glazman, and R. J. Schoelkopf, “Ten milliseconds for aluminum cavities in the quantum regime,” *Appl. Phys. Lett.* **102**, 192604 (2013).
- [2] M. Reagor, W. Pfaff, C. Axline, R. W. Heeres, N. Ofek, K. Sliwa, E. Holland, C. Wang, J. Blumoff, K. Chou, M. J. Hatridge, L. Frunzio, M. H. Devoret, L. Jiang, and R. J. Schoelkopf, “Quantum memory with millisecond coherence in circuit qed,” *Phys. Rev. B* **94**, 014506 (2016).
- [3] M. Hatridge, R. Vijay, D. H. Slichter, J. Clarke, and I. Siddiqi, “Dispersive magnetometry with a quantum limited SQUID parametric amplifier,” *Phys. Rev. B* **83**, 134501 (2011).
- [4] T. Roy, S. Kundu, M. Chand, A. M. Vadiraj, A. Ranadive, N. Nehra, M. P. Patankar, J. Aumentado, A. A. Clerk, and R. Vijay, “Broadband parametric amplification with impedance engineering: Beyond the gain-bandwidth product,” *Appl. Phys. Lett.* **107**, 262601 (2015).
- [5] A. Kamal, A. Marblestone, and M. H. Devoret, “Signal-to-pump back action and self-oscillation in double-pump Josephson parametric amplifier,” *Phys. Rev. B* **79**, 184301 (2009).
- [6] K. W. Murch, S. J. Weber, C. Macklin, and I. Siddiqi, “Observing single quantum trajectories of a superconducting quantum bit,” *Nature* **502**, 211 (2013).
- [7] N. Ofek, A. Petrenko, R. Heeres, P. Reinhold, Z. Leghtas, B. Vlastakis, Y. Liu, L. Frunzio, S. M. Girvin, L. Jiang, M. Mirrahimi, M. H. Devoret, and R. J. Schoelkopf, “Extending the lifetime of a quantum bit with error correction in superconducting circuits,” *Nature* **536**, 441 (2016).
- [8] S. E. Nigg, H. Paik, B. Vlastakis, G. Kirchmair, S. Shankar, L. Frunzio, M. H. Devoret, R. J. Schoelkopf, and S. M. Girvin, “Black-box superconducting circuit quantization,” *Phys. Rev. Lett.* **108**, 240502 (2012).
- [9] N. Khaneja, T. Reiss, C. Kehlet, T. Schulte-Herbrüggen, and S. J. Glaser, “Optimal control of coupled spin dynamics: design of nmr pulse sequences by gradient ascent algorithms,” *Journal of magnetic resonance* **172**, 296 (2005).
- [10] P. De Fouquieres, S. Schirmer, S. Glaser, and I. Kuprov, “Second order gradient ascent pulse engineering,” *Journal of Magnetic Resonance* **212**, 412 (2011).
- [11] A. P. Sears, A. Petrenko, G. Catelani, L. Sun, H. Paik, G. Kirchmair, L. Frunzio, L. I. Glazman, S. M. Girvin, and R. J. Schoelkopf, “Photon shot noise dephasing in the strong-dispersive limit of circuit qed,” *Phys. Rev. B* **86**, 180504(R), (2012).
- [12] A. Blais, R.-S. Huang, A. Wallraff, S. M. Girvin, and R. J. Schoelkopf, “Cavity quantum electrodynamics for superconducting electrical circuits: An architecture for quantum computation,” *Phys. Rev. A* **69**, 062320 (2004).
- [13] L. Sun, A. Petrenko, Z. Leghtas, B. Vlastakis, G. Kirchmair, K. M. Sliwa, A. Narla, M. Hatridge, S. Shankar, J. Blumoff, L. Frunzio, M. Mirrahimi, M. H. Devoret, and R. J. Schoelkopf, “Tracking photon jumps with repeated quantum non-demolition parity measurements,” *Nature* **511**, 444 (2014).
- [14] F. Motzoi, J. M. Gambetta, P. Rebentrost, and F. K. Wilhelm, “Simple pulses for elimination of leakage in weakly nonlinear qubits,” *Phys. Rev. Lett.* **103**, 110501 (2009).
- [15] W. Wang, L. Hu, Y. Xu, K. Liu, Y. Ma, S.-B. Zheng, R. Vijay, Y. P. Song, L.-M. Duan, and L. Sun, “Converting quasiclassical states into arbitrary fock state superpositions in a superconducting circuit,” *Phys. Rev. Lett.* **118**, 223604 (2017).
- [16] M. H. Michael, M. Silveri, R. T. Brierley, V. V. Albert, J. Salmilehto, L. Jiang, and S. M. Girvin, “New Class of Quantum Error-Correcting Codes for a Bosonic Mode,” *Phys. Rev. X* **6**, 031006 (2016).
- [17] J. R. Johansson, P. D. Nation, and F. Nori, “Qutip: An open-source python framework for the dynamics of open quantum systems,” *Comp. Phys. Comm.* **183**, 1760 (2012).
- [18] J. R. Johansson, P. D. Nation, and F. Nori, “Qutip 2: A python framework for the dynamics of open quantum systems,” *Comp. Phys. Comm.* **184**, 1234 (2013).

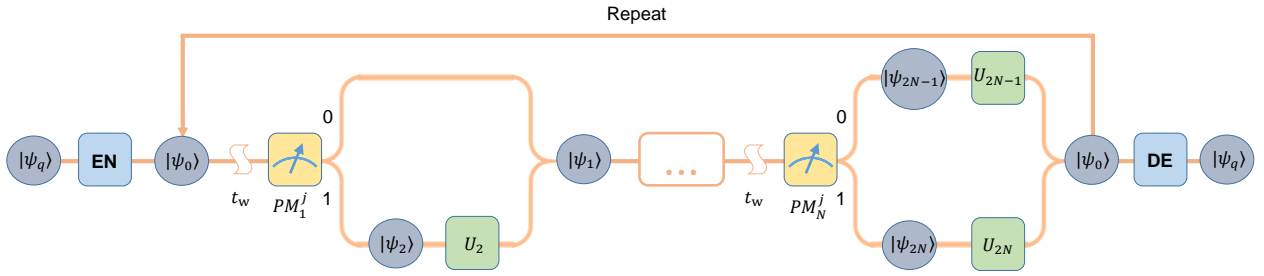


FIG. S13. **Protocol with more bottom-layer QEC steps.** When no error is detected, the state after the deterministic evolution should be untouched as much as possible to minimize the errors induced by the recovery gates. This can potentially increase the QEC protected lifetime.

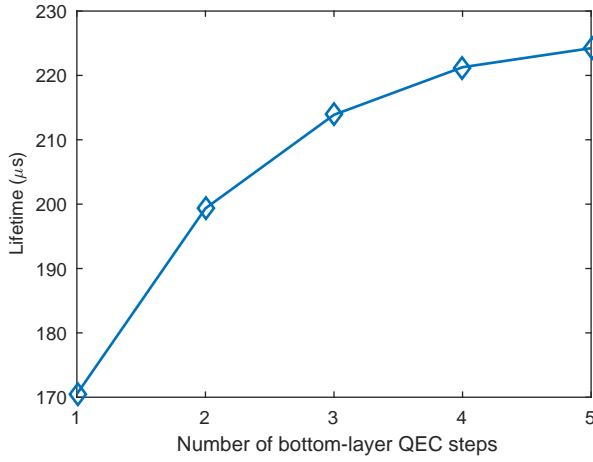


FIG. S14. **Dependence of the logical qubit lifetime on the number of bottom-layer QEC steps.** The lifetime is extended when the number of bottom-layer QEC steps is increased, because the state after the deterministic evolution is untouched as much as possible when no error is detected and thus fewer errors are introduced.